REVIEW

Biomedical Engineering Communications 2022;1(1):3. https://doi.org/10.53388/BMEC2022003

Recent developments of fluorescence imaging technology in the second near-infrared window

Shu-Tong Wu[1#], Lin Chen[1#], Wei-Wei Kang[1], Qin Liu[1], Meng-Ting Gao[1], Dong-Sheng Li[1], Yao Li[1], Rong Dai[1], Zi-Liang Zheng[1*]

[1]Institute of Medical Technology, Shanxi Medical University, Taiyuan, 030001, China.

[#]Shu-Tong Wu and Lin Chen are the co-first authors for this paper.

[*]**Corresponding to:** Zi-Liang Zheng, Institute of Medical Technology, Shanxi Medical University, No. 56, Xinjiannan Road, Yingze, Taiyuan, 030001, China. E-mail: zzlsxty@sina.com.

Author contributions

Conceptualization, Zi-Liang Zheng; Investigation, Shu-Tong Wu, Lin Chen, and Wei-Wei Kang; Writing-Original Draft, Shu-Tong Wu and Lin Chen;Writing Review & Editing, Qin Liu, Meng-Ting Gao, Dong-Sheng Li, and Rong Dai; Supervision, Zi-Liang Zheng. All authors read and discussed the manuscript.

Competing interests

The authors declare no conflicts of interest.

Acknowledgments

This work was supported by the National Natural Science Foundation of China (82102124, 82071987, 81771907, 8211001138, 8210072688), Science and technology innovation team project of Shanxi Province (201705D131026), Engineering Technology Research Center of Shanxi Province (201805D121008), Scientific and technological achievements transformation project of Shanxi Province (201704D131006), Laboratory Construction Project of Shanxi Province, the Projects for Local Science and Technology Development Guided by the Central Committee (YDZX20191400002537), Research Project Supported by Shanxi Scholarship Council of China (2020-177), Fund Program for the Scientific Activities of Selected Returned Overseas Professionals in Shanxi Province (20200006); Four Batches of Scientific Research Projects of Shanxi Provincial Health Commission (2020TD11, 2020SYS15, 2020XM10); Key Laboratory of Nano-imaging and Drug-loaded Preparation of Shanxi Province (NO: 202104010910010), Shanxi Province Science Foundation for Youths (201901D211343).

Abbreviations

SBR, signal-to-background ratio; NIR-I FLI, Near-Infrared-I Fluorescent Imaging; FDA, Food and Drug Administration; ICG, Indocyanine green; NIR-II FLI, Near-Infrared-II Fluorescent Imaging; NIR-IIa, near-infrared II; NIR-IIb, near-infrared IIb; QYs, quantum yields; SWCNTs, single-walled carbon nanotubes; H_2O_2, hydrogen peroxide; NO, nitric oxide; SNR, signal-to-noise ratio; QDs, quantum dots; SNR, signal-to-noise ratio; hMSCs, human mesenchymal stem cells; PTT, photothermal therapy; PLQY, photoluminescence quantum yield; $ONOO^-$, Peroxynitrite; TBI, Traumatic brain injury; RENPs, Rare-earth doped nanoparticles; NaBH4, sodium borohydride; AIE, Aggregation-induced Emission; BBTD, benzobisthiadiazole; D-A-D, donor-acceptor-donor; BODIPY, Dipyrromethene Boron Difluoride; PCP, paracyclophane; SPNs, semiconducting polymer nanoparticles.

Peer review information

Biomedical Engineering Communications thanks all anonymous reviewers for their contribution to the peer review of this paper.

Citation

Wu ST, Chen L, Kang WW, et al. Recent Developments of Fluorescence Imaging Technology in the Second Near-Infrared Window. *Biomed Eng Commun*. 2022;1(1):3. doi: 10.53388/BMEC2022003.

Executive editor: Xin-Yun Zhang.

Received: 19 September 2022; **Accepted:** 20 October 2022; **Available online:** 26 October 2022.

Abstract

Background: Fluorescence bio-imaging in the second near-infrared window (NIR-II FL, 1000–1700nm) has great potential in clinical theranostics, which is of great importance providing precise locations of lesions and molecular dynamic actions simultaneously in a single nanoprobe. **Methods:** There has been an upsurge of multidisciplinary research focusing on developing functional types of inorganic and organic nanoprobes that can be used for NIR-II FL with the high spatiotemporal resolution, deep tissue penetration, and negligible auto-fluorescence. **Results:** In this mini-review, we summarize recent progress in inorganic/organic NIR-II FL nanoprobes. We introduce the design and properties of inorganic and organic nanoprobes, in the order of single-walled carbon nanotubes, quantum dots, rare-earth-doped nanoparticles, metal nanoclusters and organic fluorophores, expect to realize precise diagnosis and efficient image-guided therapy. **Conclusion:** Meanwhile, to elucidate the problems and perspectives, we aim to offer diverse biological applications of inorganic/organic NIR-II FL nanoprobes and accelerate the clinical transformation progress.

Keywords: second near-infrared biowindow; NIR-II fluorescence bio-imaging; organic nanoprobes; inorganic nanoprobes; imaging performance

Introduction

In the past decades, several noninvasive imaging technologies have been developed for both scientific research and clinical applications, such as single-photon-emission CT, positron emission tomography, computed tomography, magnetic resonance imaging and ultrasound imaging [1–3]. However, influenced by low sensitivity, high ionizing radiation, and long inspection time, these traditional imaging modalities are challenging to satisfy the increasing demand of precise theranostics [4, 5].

Optical imaging has attracted considerable attention owing to its high sensitivity, fast feedback, low damage, non-radioactivity, and high spatial and temporal resolution [6, 7]. So far, visible (400–700 nm) and NIR (700–1700 nm) imaging have been applied into clinical practice. For instance, clinical applicability has been presented in sentinel lymph node mapping, visualization of the vascularization process, and topical tumor imaging [8, 9]. However, the visible imaging has some limitations like inadequate penetration depth, high tissue scattering and endogenous substances auto-fluorescence [10, 11]. Therefore, it is of great importance to acquire a novel imaging modality. Compared with visible imaging, reduced photon scattering and auto-fluorescence in the NIR region remarkably assured high temporal and spatial resolution and signal-to-background ratio (SBR) (Figure 1D) [12–14].

Near-Infrared-I Fluorescent Imaging (NIR-I FLI, 700–900 nm) has been widely utilized for the visualization of organs and tissues of human body, such as blood vessels and cancerous tissue as well as clinical preoperative diagnosis and intraoperative navigation [15, 16]. United States Food and Drug Administration (FDA) has approved several surgical grade image-guided systems, including SPY Elite (Novadaq), PDE (Hamamatsu), SPY PHI (Novadaq), and Fluobeam (Fluoptics) [17]. Indocyanine green (ICG) and methylene blue as NIR-I FLI nanoprobes, approved by the FDA more than 50 years ago, that have been used in NIR FLI intraoperative imaging for visualization of anatomical structures [18–21]. Remarkably, the Near-Infrared-II Fluorescent Imaging (NIR-II FLI, 1000–1700 nm) exhibits great potential for clinical applications due to its recognized higher resolution and SBR, lower autofluorescence and deeper biological tissue penetration capability compared to visible and NIR-I FL (Figure 1) [22–24]. Furthermore, the NIR-II FLI has been divided into two subranges: near-infrared IIa (NIR-IIa, 1000–1400 nm) and near-infrared IIb (NIR-IIb, 1500–1700 nm) [25, 26]. It is well known that evolving NIR-II FL system promotes the development of NIR-II FL nanoprobes [27–29]. Increasing nanoprobes with excellent properties are occurred to satisfy the requirements of precise and efficient early diagnosis and prognosis.

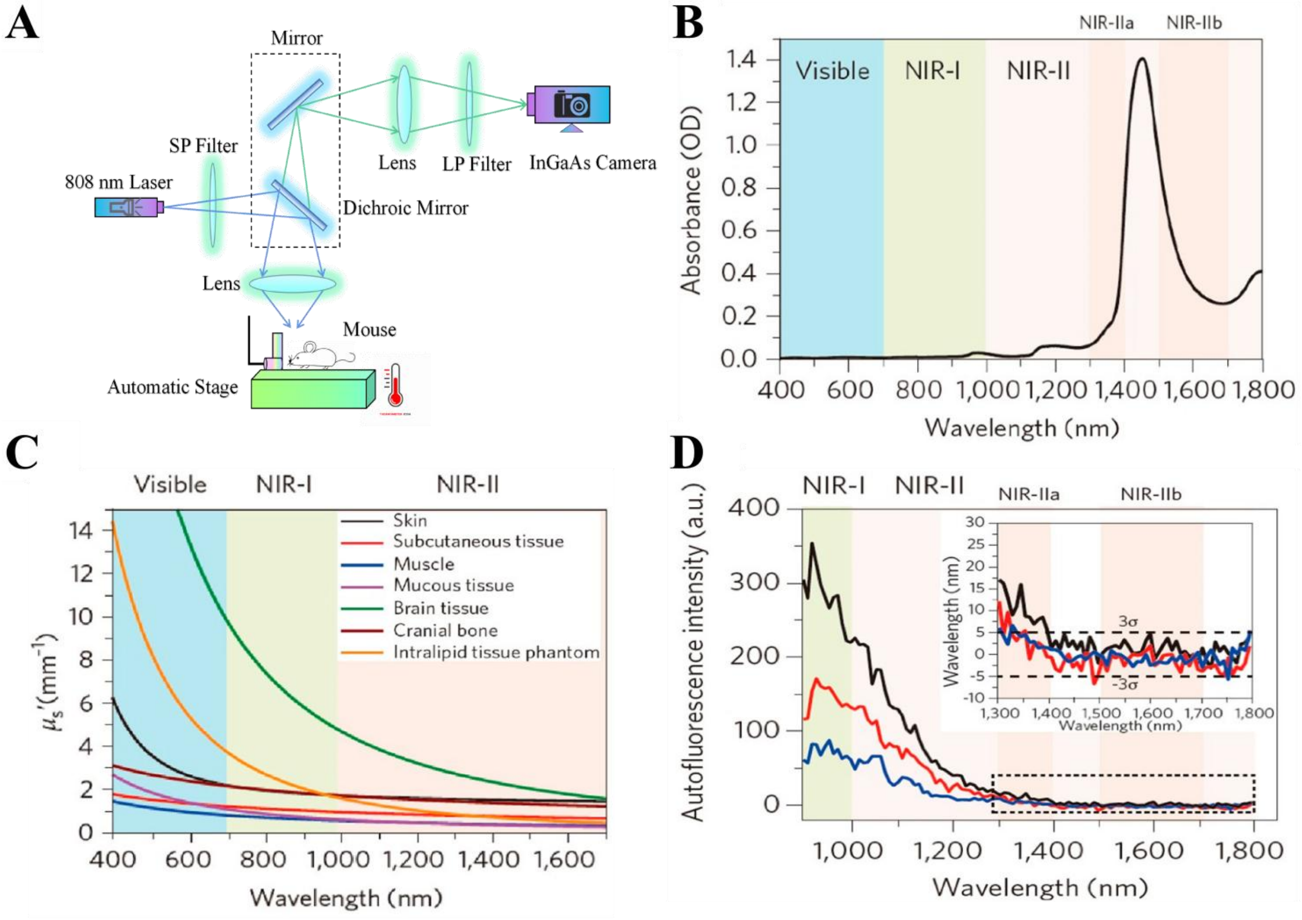

Figure 1 (A) A schematic of the imaging setup for NIR-II photons using InGaAs cameras. (B) Absorption spectrum of water through a 1-mm-long path. OD, optical density. (C) The reduced scattering coefficient, μs’, is plotted as a function of wavelength in the range of 400–1700 nm for various tissue types including the skin (black), the mucous tissue (red), muscle (blue), skull (pink), the brain tissue (green), and the tissue phantom, Intralipid (orange). Please note that the plots for skin, mucous tissue, muscle, and skull are derived from human samples, while that for brain is derived from mouse sample. The ranges of visible, NIR-I, and NIR-II windows in the spectrum are also shaded in light blue, green, and red, respectively. Reproduced with permission. Hong G, Diao S, Antaris AL, et al. Carbon Nanomaterials for Biological Imaging and Nanomedicinal Therapy. *Chem Rev* 2015;115(19):10816–10906. Copyright 2015, Springer Nature. (D) Autofluorescence spectra of ex vivo mouse liver (black), spleen (red) and heart tissue (blue) under 808-nm excitation light, showing the absence of autofluorescence in the >1,500 nm NIR-II window. Reproduced with permission. Hong G, Antaris AL, Dai H. Near-infrared fluorophores for biomedical imaging. *Nat Biomed Eng* 2017;1(1):0010. Copyright 2017, Springer Nature. NIR-II, Near-Infrared-II; NIR-I, Near-Infrared-I; NIR-IIa, Near-Infrared IIa; NIR-IIb, Near-Infrared IIb.

The excitation light source, emission light tracker and image-forming optical system are required to acquire the spatiotemporal distribution of fluorescent nanoprobes labeled tissues and anatomical structures. When the excitation photons reach the fluorescent nanoprobe and excite it, the nanoprobe will emit photons which detected by image-forming instrumentation. Therefore, the nonspecific reflection of surface interface and components of animal tissue greatly hampered the process of photons. Besides these reflections, in-tissue absorption and tissue autofluorescence are included in the process. Melanins, reduced nicotinamide adenine dinucleotide and flavins have specific absorption and autofluorescence in the short wavelength spectrum [14]. The introduction of NIR-IIb FLI by Dai et al. provides the autofluorescence-free and minimal tissue scattering window for biological imaging [17, 25]. In this process, what's the most important is to develop a versatile nanoprobe that enables specific targeting and biocompatibility. In 2009 Dai and his colleagues first developed phospholipid-polyethylene glycol coated nanotubes via the surfactant exchange method to visualize tumor vessels under NIR-II FLI. Numerous inorganic/organic nanoprobes have been developed for NIR-II FLI to realize precise tumor recognition, specific molecule detection and visualization of drug delivery process [24, 30]. Currently, Tian et al. have developed a multi-modality imaging nanoplatform that integrated visible and NIR-I/II FLI to accomplish the first NIR-I/II FL guided in-human liver resection surgery. This work aimed to show that NIR-II FLI has great potential over traditional NIR-I FLI imaging in clinical intraoperative navigation [31].

The clinical transformation of NIR-II FL nanoprobes requires excellent biocompatibility, high quantum yields (QYs), easy metabolism and well-refined structure (Figure 2) [32–34]. In recent years, many NIR-II FL nanoprobes have been constructed for preclinical disease diagnosis, image-guided surgery or combination therapy [35–37]. Herein, the NIR-II FL nanoprobes are divided into inorganic nanoprobes and organic nanoprobes, aiming to provide an overview of their imaging properties and biological applications, respectively.

Inorganic Nanoprobes

Single-Walled Carbon Nanotubes (SWCNTs)

Carbon nanomaterials are a kind of low-dimensional materials that have a great number of unique chemical and photophysical properties [24]. All carbon nanomaterials, including carbon nanotubes, graphene40and carbon dots can exhibit fluorescence properties owing to their normal Stokes shift [38–42]. It is worth noting that the larger Stokes shift causes SWCNTs to be excited in the first NIR-I window and can be detected in the NIR-II window [43].

A single-walled carbon nanotube can be considered as a single graphene sheet rolled up seamlessly into a cylinder with its diameter mostly less than 2 nm. Since Smalley and Weisman et al. reported that SWCNTs could emit NIR fluorescence due to their wide band gap in 2002, it has attracted a great deal of interest around the world [6]. Then, Dai and coworkers developed a biocompatible SWCNT with strong NIR-II FL, which achieved whole-animal NIR-II FLI for the first time (Figure 3A–B) [30]. Later, the SWCNTs have gradually applied to various diseases models, such as peripheral arterial diseases, bacterial infection, lymphatic vessel imaging of tumor metastasis and imaging guided tumor resection surgery [44–47]. Besides structural imaging of different disease, the NIR-II FL of SWCNTs has been considered as optical biosensors, allowing unique detection of certain molecular species such as hydrogen peroxide (H_2O_2) and nitric oxide (NO) (Figure 3C) [48, 49]. Strano's group has reported a series of methods to detect the biomarkers of versatile diseases. NIR-II fluorescent SWCNTs were coated with DNA oligonucleotides which can select NO especially, enabling the selective detection of local nitric oxide concentration of inflamed liver with a detection limit of 1 mM [48]. The fluorescence of SWCNT can be immediately quenched due to the reaction of NO radical with DNA oligonucleotides. The NO biosensor based on fluorescent SWCNT could be used to investigate tissue inflammation activity and cell signaling pathways.

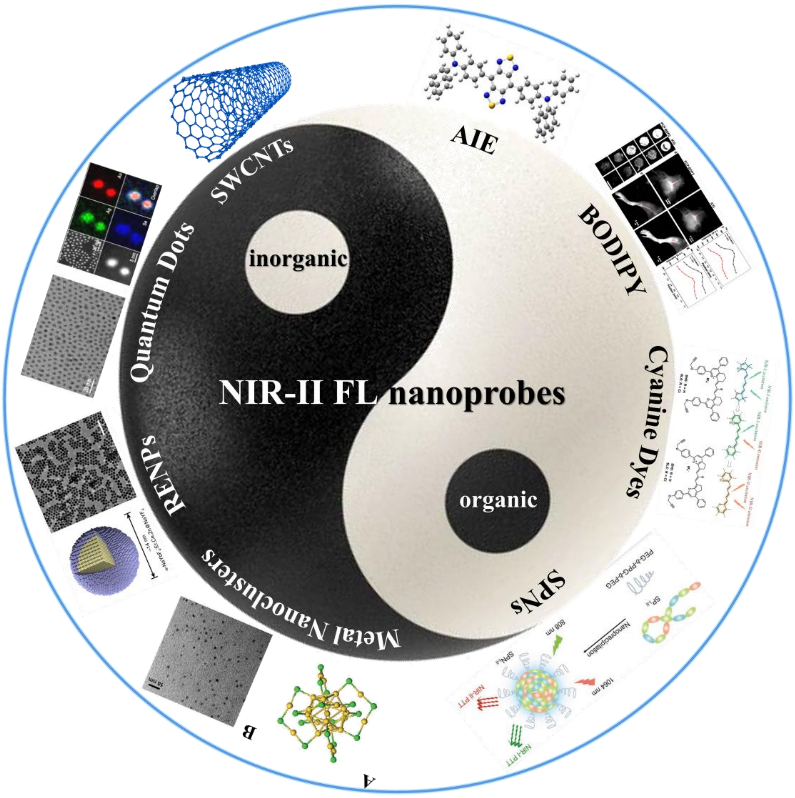

Figure 2 Schematic illustration of NIR-II Fluorescent Probe. NIR-II, Near-Infrared-II.

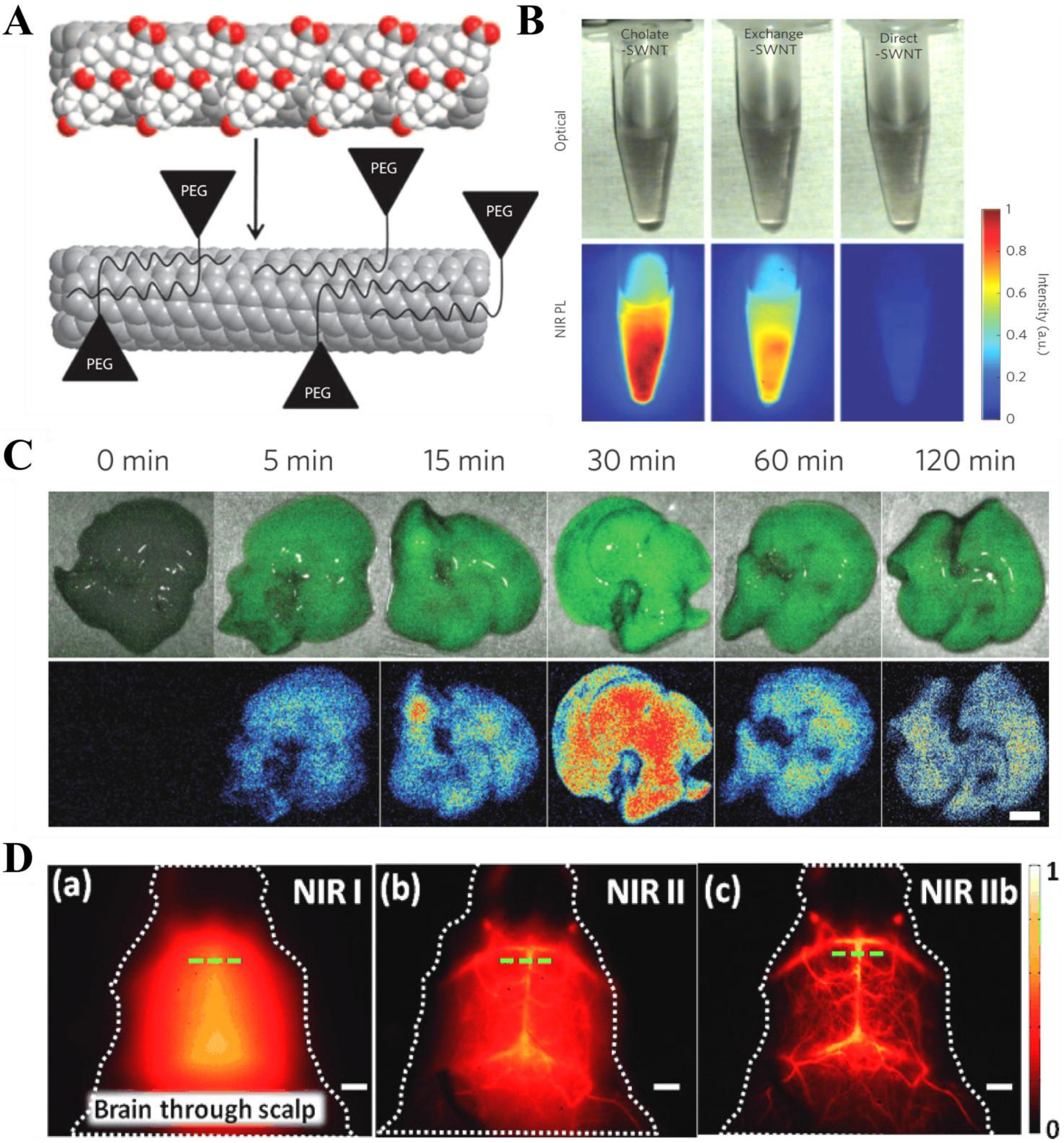

Figure 3 (A) Schematic of the exchange process. Cholate (red and white balls) on SWNTs (grey) is dialysed and eventually replaced by phospholipid–polyethylene glycol (PL–PEG) to form biocompatible nanotubes without damaging the integrity of the nanotube sidewall. (B) NIR photoluminescence images of the three solutions excited at 808 nm at equal concentrations. Exchange-SWNTs show greater fluorescence yield than direct-SWNTs. Reproduced with permission. Welsher K, Liu Z, Sherlock SP, et al. A route to brightly fluorescent carbon nanotubes for near-infrared imaging in mice. *Nature Nanotech* 2009;4(11):773–780. Copyright 2009, Springer Nature. (C) Images of excised livers deconvoluted with 2D technology showing PEG-(AAAT)7-SWNT localization relative in the liver (top) and a heatmap of fluorescence (bottom; scale bar, 4 mm). Reproduced with permission. Iverson NM, Barone PW, Shandell M, et al. In vivo biosensing via tissue-localizable near-infrared-fluorescent single-walled carbon nanotubes. *Nature Nanotech* 2013;8(11):873–880. Copyright 2009, Springer Nature. (D) Fluorescence images of the cerebrovascular of mice (n = 2) without craniotomy in the NIR-I (a), NIR-II (b), and NIR-IIb (c) regions. Scale bars: 2 mm. Reproduced with permission. Diao S, Blackburn JL, Hong G, et al. Fluorescence Imaging In Vivo at Wavelengths beyond 1500 nm. *Angew Chem Int Ed* 2015;54(49):14758–14762. Copyright 2015, Wiley-VCH. NIR-II, Near-Infrared-II; NIR-I, Near-Infrared-I.

Moreover, SWCNTs were used as imaging contrast agents in the NIR-IIb window., which reduced tissue autofluorescence and increased signal-to-noise ratio (SNR) compared to the NIR-IIa window. Dai et al. developed a modified laser vaporization method to synthesize fluorescent SWCNT in the NIR-IIb window (Figure 3D) [50]. This kind of SWCNT can be used as brain vessel imaging at depths of up to 3 mm through the intact skull of C57Bl/6 mice. Surprisingly, the signal-to-background ratios of the NIR-IIb window were higher than that for the NIR-I and NIR-IIa windows, suggesting that the minimized photon scattering and higher SBRs in the NIR-IIb region.

Quantum Dots (QDs)

The tunable emission wavelength, high quantum yield, excellent water solubility and ultra-small size make quantum dots ideal fluorescent nanoprobes in biomedical field [51, 52]. Numerous QDs can be classified as different formation methods and elemental compositions. For example, a large number of QDs include the following classes in terms of elements of different groups: IV (Si, Ge), IV-VI (PbS, PbSe), III-V (InAs, InSb), II-VI (HgSe, HgTe), I-VI (Ag_2S, Ag_2Se, Ag_2Te), and I-III-VI ($CuInS_2$, $AgBiS_2$, $AgInSe_2$) etc [10]. NIR-II QDs can be successfully used as imaging agents for cells, tumor sites, lymphoid tissues, and blood vessels. Among them, silver chalcogenide QDs including silver sulfide (Ag_2S), silver telluride (Ag_2Te), and silver selenide (Ag_2Se), have good biocompatibility because of their low toxicity components to biological systems [53]. The biocompatibility of Ag_2S QDs can be proved through the labeling of human mesenchymal stem cells (hMSCs) in vivo by Wang and his co-workers [54]. The Ag_2S could be used as a fluorescent probe with high sensitivity, in which 1000 Ag_2S-QDs labeled hMSCs can be tracked in vivo. Those Ag_2S-QDs marked hMSCs could maintain the fluorescence intensity for up to 30 days after injection without any interference of stem cell proliferation. Remarkably, Ag_2S-QDs labeled hMSCs' distribution inliver and lung could be detect dynamically under NIR-II FL up to 14 days. Moreover, Ag_2S QD has been widely applied to cancer imaging, vessel imaging, and lymphatic imaging [55]. For instance, Zheng et al. have constructed Ag_2S-GOx@BSA-hollow SiO_2 based on a novel one-step dual-template synthesis, which could achieve NIR-II FL and photoacoustic imaging-guided photothermal therapy (PTT) (Figure 4A–D) [56]. Ag_2S QD was synthesized through the biomineralization approach and can be catalyzed to release Ag^+ in the tumor microenvironment to realize ion therapy.

Wang and coworkers reported a novel solvothermal method to synthesize Ag_2Se QDs with emission at 1300nm [57]. Ag_2Se QDs are further performed in the deep tissue imaging of organs and blood vessels. Compared with traditional fluorescent dye ICG, Ag_2Se QDs not only can track small vessels with a diameter of 123 μm, but also show minimal tissue autofluorescence and deep penetration. However, the low photoluminescence quantum yield (PLQY) of NIR-II QDs is still a challenge to researchers compared to visible-emission QDs, whose PLQY can be near-unity. To solve this issue, Wang and co-workers recently reported the alloyed QDs with enhanced PLQY in the NIR-II window (Figure 4E–G) [58]. They synthesized AgAuSe QDs by an imperative alloying method. The PLQY of AgAuSe QDs could be up to 65.3 % at 978 nm for the first time. Besides this, the lifetime of AgAuSe QDs is 4.58 μs and the photoluminescence emission is removed to 1170 nm in the NIR-II biological window. In this synthesis route, the lattice diffusion of the Au atom in Ag_2Se QDs activated the conversion from Ag_2Se to AgAuSe QDs. This novel alloying strategy exhibited great potential in bioimaging in the NIR-II window. Furthermore, Wang et al. developed an "off-on" Ag_2S QDs to track peroxynitrite ($ONOO^-$) which originated from the cerebral vasculature (Figure 4H–I) [59]. To the best of our knowledge, $ONOO^-$ plays an essential role in the progression of Traumatic brain injury (TBI). Activatable NIR-II nanoprobes V&A@Ag_2S QDs are composed of a NIR absorber A1094 and VCAM1 binding peptide except for NIR-II fluorescent emitter Ag_2S. A1094 chromophore could be oxidized by the overload $ONOO^-$ in the TBI region, and served as an energy acceptor. The fluorescent Ag_2S QDs nanoprobe is "turned off" during the absorption of A1094. It can be "turned on" only if A1094 is oxidized by a high $ONOO^-$ level in the TBI mice model.

Moreover, many researchers explored novel fluorescent nanoprobes in the NIR-IIb even NIR-IIc (1700–2000nm) biological window. Dai and his team reported a sulfide/cadmium sulfide quantum dots emitting at ~1880nm and detected by a superconducting nanowire single-photon detectors up to 2,000 nm [60]. NIR-IIc FLI can further suppress light scattering and visualize mouse scalp/skull/brain structures accurately. PbS QDs with an emission peak at ~2009 nm are synthesized via a modified organometallic method. After a CdS shell grown up outside the PbS core, the emission peak shifted to ~1880 nm. Following tail-vein injection of PbS/CdS QDs into the mouse, three-dimensional intact mouse scalp/skull/brain could be seen by NIR-IIc confocal microscopy. Peripheral node address on high endothelial venules play an important role in cancer immunological reaction. This PbS/CdS QDs could mapped out Peripheral node address on high endothelial venules, which discriminate tumor molecule such as CD169 and CD3 in a living body. The strategy enables non-invasive, surgery-free molecular imaging of tumor inside mouse in NIR-IIc window.

Rare-earth doped nanoparticles (RENPs)

RENPS mainly were constructed with core-shell structure, the core includes the main substance and dopants, and the undoped host material wraps the core to be a shell. Due to the rare-earth elements which exhibit various energy level transitions, RENPs also possess efficient downconversion NIR-II emission except for the visible/NIR-I upconversion emission [61, 62]. In recent years, RENPs has been benefited from diverse emission wavelength, extendable half-lifetime of luminescence, and nonphotobleaching activity. In 2013, P.V. Moghe and co-workers suggested the first RENPs for in vivo NIR-II FL imaging and disease detection [63]. These kinds of RENPs were synthesized based on a core-shell structure consisting of a rare-earth-doped $NaYF_4$ core and surrounded by an undoped $NaYF_4$ shell. Through doping the $NaYF_4$ with different RE elements such as ytterbium (Yb), erbium (Er), holmium (Ho), thulium (Tm) or praseodymium (Pr), RENP changed the emission wavelength remarkably. This kind of novel RENP nanoprobes could realize tumor imaging with tunable emission wavelength and higher detection sensitivity. Furthermore, Cheng's group developed a DSPE-PEG coated RENP for bone disease imaging because its unique affinity to hydroxyapatite (Figure 5A–C) [64]. Besides skeletal system mapping, RENPs@DSPE-mPEG has been successfully applied to the lymph nodes and blood vessels imaging in vivo.

The luminescence of RENPs can be enhanced by alkaline metal dopants such as Na^+, K^+ or $Zn2^+$ and Mn^{2+}. Recently, Dai and co-workers developed a novel kind of $NaYF_4$ downconversion NPs through doping Zn^{2+} ions into the cubic-phase α-ErNPs for tumor imaging (Figure 5D–G) [65]. The downconversion NPs achieved a total 11-fold luminescence by enhancing multi-phonon relaxation and reducing crystal field symmetry. This work developed an ultra-bright Zn^{2+} ion doping downconversion Er NPs for NIR-IIb FL for the first time. In addition, Tian et al. constructed a multifunctional lanthanide NP coated with liposome, which exhibits three emission wavelengths of fluorescence including NIR-II, NIR-IIa and NIR-IIb under the excitation of 808 nm at the same time [32]. The lanthanide NPs synthesized by a thermal decomposition method, Yb^{3+}/ Er^{3+} ion pair, Yb^{3+} ion, and Nd^{3+} ion located in their core, the second and the third shell, respectively. Due to the different lanthanide elements having diverse excited states and energy transfer processes, the NPs display three fluorescence emission peaks situated at 1064 nm, 1325 nm and 1542 nm corresponding to NIR, NIR-IIa and NIR-IIb biological windows. Then, the outermost liposome shell was used to improve biocompatibility and water solubility. Notably, the nanoprobes can detect the brown adipose tissue without any targeting molecules, for which the brown adipose tissue is related to many metabolic diseases. The RE nanoprobes could also be used for circulatory system imaging and intraoperative image-guided surgery. In this way, it is of great importance to develop RENPs as multifunctional NIR-II FL nanoprobes in the diagnosis of many diseases.

Metal Nanoclusters

Metal nanoclusters are composed of different metal atoms with specific spatial coordination. Metal nanoclusters are famous for ultra-small sizes around 1–3 nm and tunable atomic structures. Metal nanoclusters can be divided into gold clusters and silver clusters according to the type of the primary element. It can also fall into different groups such as mono-metallic clusters, bimetallic clusters and polymetallic clusters. Since gold nanoclusters are reported for their unique luminescence, it is of great importance to develop a gold clusters with stable atomic spatial coordination and NIR-II fluorescence [66]. Xie et al. demonstrated an Au nanoclusters are synthesized by a novel method which is the thiolated-protected Au

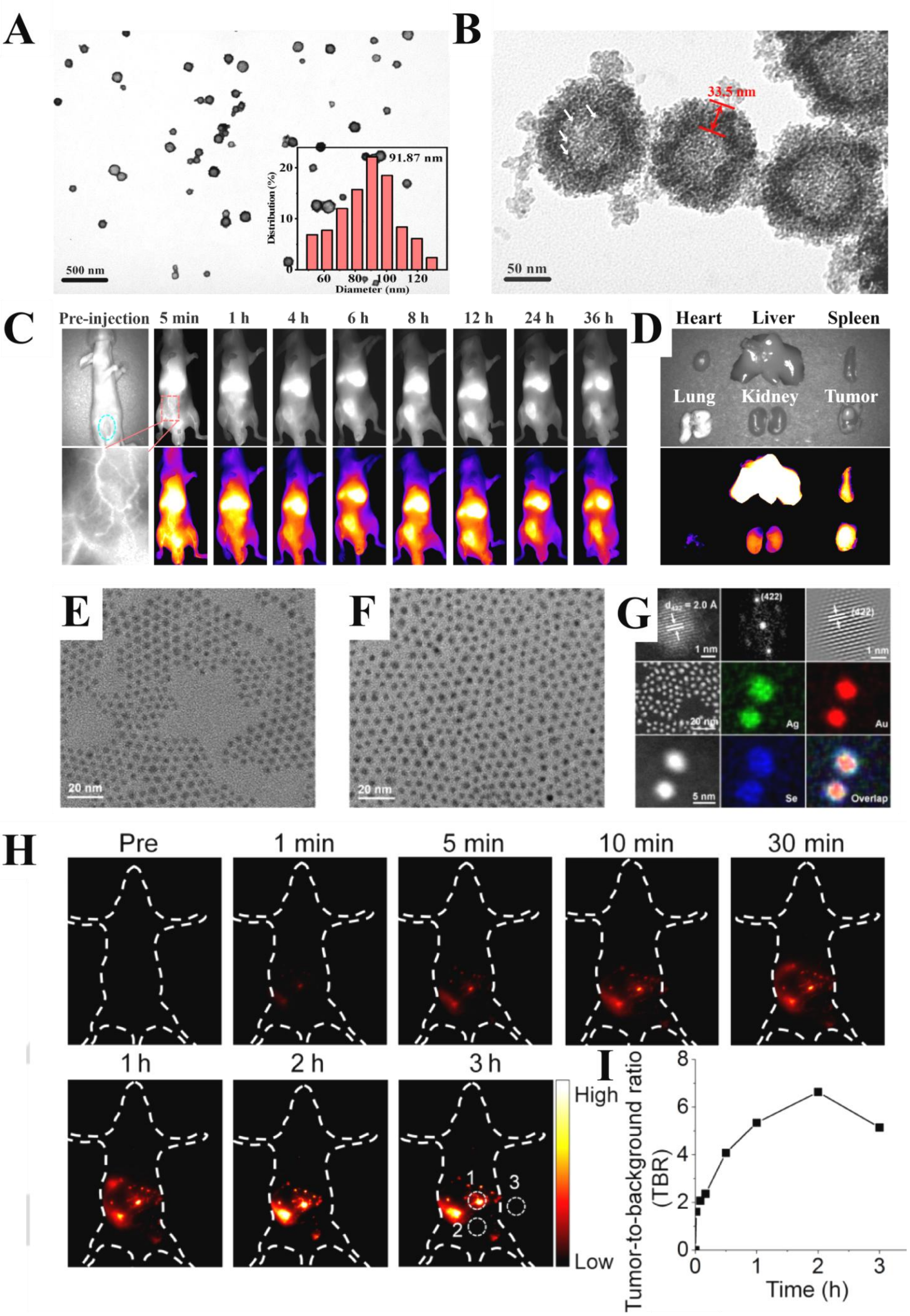

Figure 4 (A and B) TEM images of Ag$_2$S-GOx@BHS NYs at varied magnifications, where the inset is the size distribution. (C) In vivo NIR-II FL imaging (yellow circled tumor region) after intravenously injecting Ag$_2$S-GOx@BHS at varying points in time (200 μL, 500 μg mL^{-1}). The enlarged imaging of the hind limb region in (C) at 1 min. (D) NIR-II FL imaging of the isolated organs/tumor. Reproduced with permission. Hong G, Robinson JT, Zhang Y, et al. In Vivo Fluorescence Imaging with Ag$_2$S Quantum Dots in the Second Near-Infrared Region. *Angew Chem Int Ed* 2012;51(39):9818–9821. Copyright 2020, American Chemical Society. TEM images of (E) Ag$_2$Se and (F) AgAuSe QDs. (G) AC-HAADF-STEM images and corresponding EDS mappings. Reproduced with permission. Yang H, Li R, Zhang Y, et al. Colloidal Alloyed Quantum Dots with Enhanced Photoluminescence Quantum Yield in the NIR-II Window. *J Am Chem Soc* 2021;143(6):2601–2607. Copyright 2021, American Chemical Society. (H) Time course of NIR-II fluorescence images of the same mouse intraperitoneally injected with FEAD1 (I) The tumor-to-background ratio plotted as a function of time for NIR-II images. Reproduced with permission. Ling S, Yang X, Li C, et al. Tumor Microenvironment-Activated NIR-II Nanotheranostic System for Precise Diagnosis and Treatment of Peritoneal Metastasis. *Angew Chem Int Ed* 2020;59(18):7219–7223. Copyright 2021, American Chemical Society. NIR-II, Near-Infrared-II; NIR-I, Near-Infrared-I.

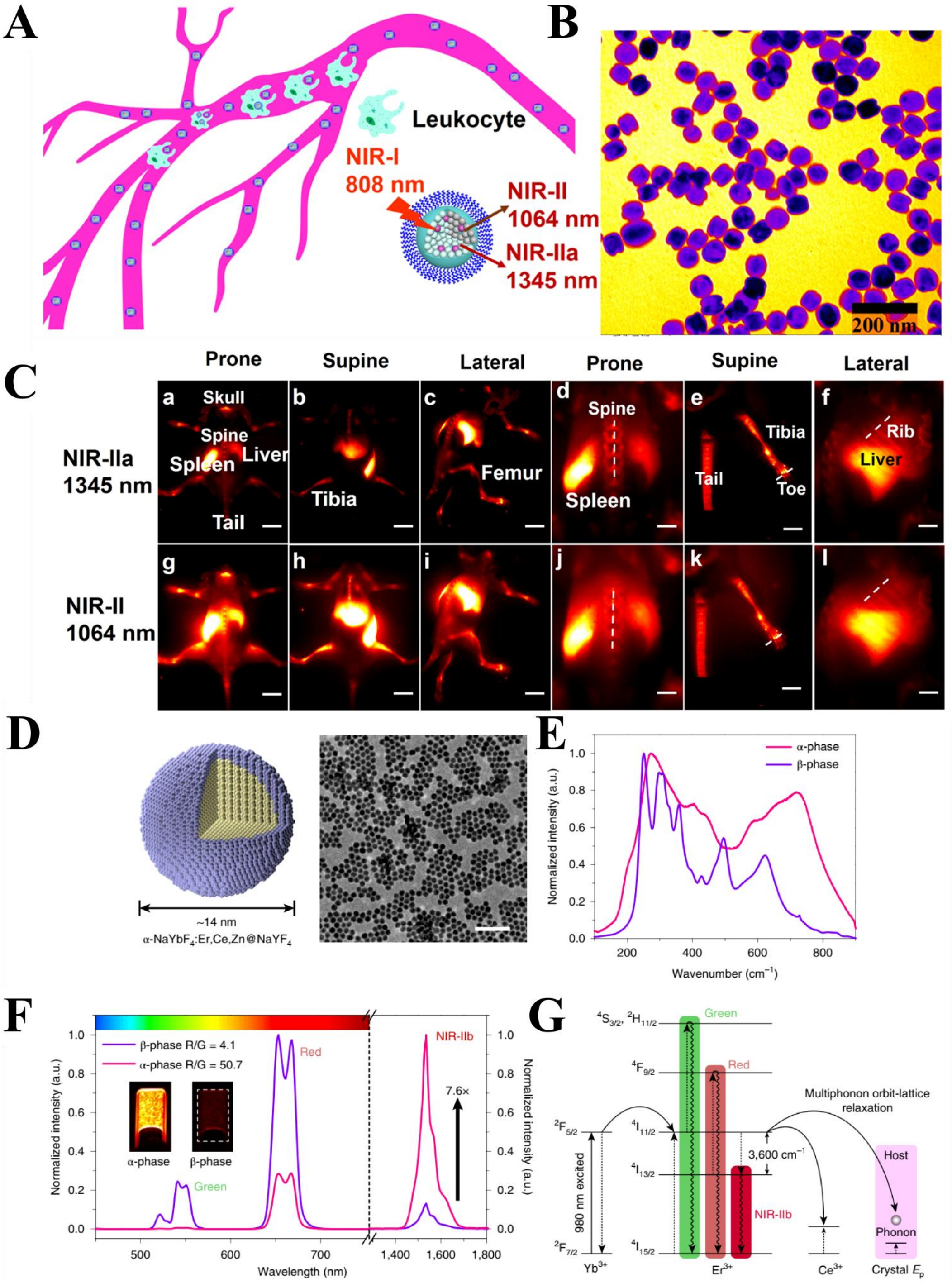

Figure 5 (A) Schematic illustration of the uptake of RENPs@DSPE-mPEG into circulating leukocytes and the schematic illustration of the RENPs@DSPE-mPEG structure with the dual NIR-II 1064 nm and NIR-IIa 1345 nm emission under 808 nm laser excitation. (B) TEM images of RENPs@DSPE-mPEG (background is yellow; DSPE-mPEG coating is red, and RENPs are blue). (C) In vivo NIR-II imaging of C57BL/6 mice (n = 3) bone in the NIR-IIa 1345 nm and NIR-II 1064 nm windows. In vivo fluorescence of the whole body in (a) prone, (b) supine, and (c) lateral postures in the NIR-IIa 1345 nm window (1250 nm long-pass filter, exposure time 500 ms) and (g) prone, (h) supine, and (i) lateral postures in the NIR-II 1064 nm window (1064 nm band-pass filter, exposure time 500 ms). Scale bar: 10 mm. High-magnification bone NIR-II imaging of the (d and j) spine, (e and k) hindpaw digits, (f and l) rib in the NIR-IIa 1345 nm window (1250 nm long-pass filter, exposure time 500 ms) and the NIR-II 1064 nm window (1064 nm band-pass filter, exposure time 500 ms). Scale bar: 5 mm. Reproduced with permission. He S, Chen S, Li D, et al. High Affinity to Skeleton Rare Earth Doped Nanoparticles for Near-Infrared II Imaging. *Nano Lett* 2019;19(5):2985–2992. Copyright 2019, American Chemical Society. (D) Schematic design of core-shell Zn-doped α-ErNPs (left) and corresponding large-scale transmission electron microscopy image (right, scale bar, 100 nm). (E) Raman spectra of cubic-phase α-ErNPs and our previously reported hexagonal-phase ErNPs34. (F) Upconversion and downconversion luminescence spectra of α-ErNPs and β-phase ErNPs. The insets show NIR-IIb luminescence images of these two nanoparticles in cyclohexane. (G) Simplified energy-level diagrams depicting the energy transfer involved in α-ErNPs on 980 nm excitation. Reproduced with permission. Zhong Y, Ma Z, Wang F, et al. In vivo molecular imaging for immunotherapy using ultra-bright near-infrared-IIb rare-earth nanoparticles. *Nat Biotechnol* 2019;37(11):1322–1331. Copyright 2019, Springer Nature. NIR-II, Near-Infrared-II; NIR-I, Near-Infrared-I; NIR-IIa, Near-Infrared IIa; RENPs, Rare-earth doped nanoparticles.

complexes can be reduced by strong reducing agents such as sodium borohydride and NaBH$_4$ or CO [67]. NIR-II FL Au clusters are composed of different atomic configurations including Au$_{25}$, Au$_{24}$, Au$_{23}$. Following this design route, Zhang's group presented a bright thiolate-protected Au$_{25}$ clusters through a metal ions doping method and surface ligand modification, whose spectra suggested that the emission wavelength is located at 1120 nm (Figure 6A–C) [68]. This novel Au clusters not only could be used in distinguishing lipopolysaccharides induced brain injury and stroke in vivo through cerebrovascular NIR-II FLI, but also could detect tumor metastasis accurately. What's more, Cheng and co-workers recently synthesized a kind of glutathione-capped gold nanoclusters Au$_{25}$(SG)$_{18}$, which can emit NIR-II FL and detect hydroxyapatite (one of the important components of bone) especially without any bone targeting ligand at the same time (Figure 6D) [69]. Au$_{25}$(SG)$_{18}$ could accumulate in the spine, knee and pelvis. Notably, the Au clusters were not gathered in the liver and spleen because of their ultra-small size, which could excrete from the body quickly after injection. Bawendi group first synthesized Au clusters capped by lipoic acid-based sulfobetaine for blood vessels imaging [70]. Through different surface modifications, AuNCs with excellent stability under versatile physiological conditions and rapid renal clearance have been synthesized.

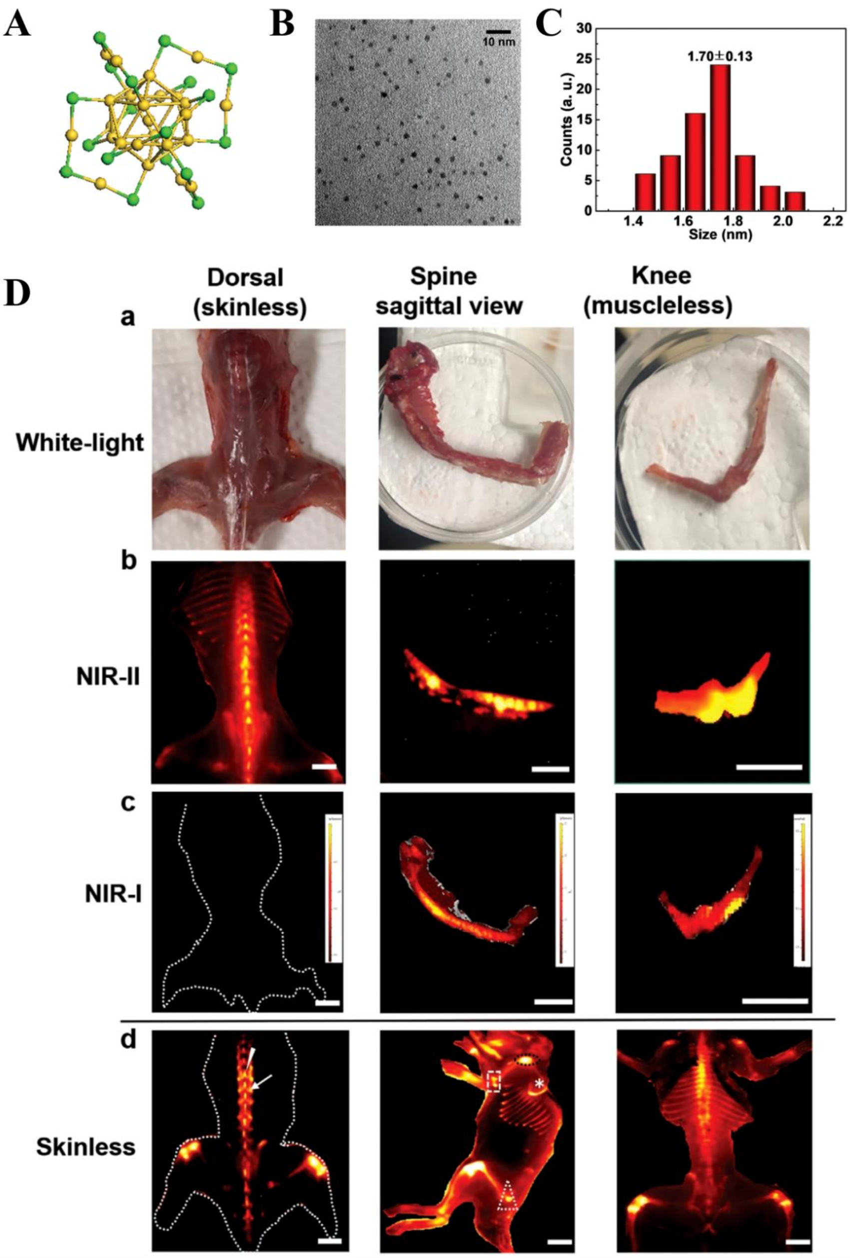

Figure 6 (A) Crystal structure of gold clusters with 25 gold atoms as core and 18 sulfur atoms. (B) Typical TEM image of gold clusters with an average size of 1.8 nm. (C) Size distribution of gold clusters obtained from TEM image. Reproduced with permission. Liu H, Hong G, Luo Z, et al. Atomic-Precision Gold Clusters for NIR-II Imaging. *Adv Mater* 2019;31(46):1901015. Copyright 2019, Wiley-ACH. (D) a) along the long axis (middle) and the muscleless knee included small part of femur and tibia (right). b) NIR-II fluorescence imaging of the above bones (1000 nm long-pass filter, exposure time 800 ms) showed obvious fluorescence in spinal processes, vertebral vertebrae, distal femur, and proximal tibia. c) NIR-I fluorescence imaging showed no fluorescence even in skinless mouse because of the limited fluorescence penetration. Fluorescence could be displayed only after fully exposing the bones (exposure time 2.5 s, binning-medium, F/stop-2, Excitation 640 nm, Emission ICG channel, lamp level-high and FOV-B). d) Another sacrificed and skinless mouse at 24 h p.i. of AuNCs (exposure time 1000 ms) showed obvious fluorescence in spinal processes (arrowhead), spinal pedicle (arrow) (left image), and all bony structures including ribs, scapula (asterisk), head of humerus (oval), elbow joint (square), and femoral head (triangle). Bar: 10 mm. Reproduced with permission. Li D, Liu Q, Qi Q, et al. Gold Nanoclusters for NIR-II Fluorescence Imaging of Bones. *Small* 2020;16(43):2003851. Copyright 2020, Wiley-VCH. NIR-II, Near-Infrared-II; NIR-I, Near-Infrared-I.

Besides Au clusters, Ag clusters can also show NIR-II fluorescence remarkably. For instance, Pradeep et al. described a new solid-state method to synthesize Ag-S nanoclusters under the protection of phosphine and hydrides, and the Ag-thiolate cluster is reduced by sodium borohydride ($NaBH_4$) [71]. Later, the discovery of bimetallic nanoclusters provided an opportunity to substitute the gold atoms in the Au-M (such as Pd, Pt, Ag, and Cu) structures. This mono or bimetallic or multi-metallic nanoclusters now can be used in chemical catalysis or sensing, optical imaging, biological labeling and drug delivery [72].

Organic nanoprobes

Aggregation-induced Emission (AIE) Luminogens

AIE is a kind of phenomenon which refers to a series of fluorophores showing weak fluorescence except for in aggregation state in the molecular structure. Therefore, AIE luminogens in NIR-II biological window allow for application at a high concentration demonstrating high spatial/temporal resolution and high signal-to-noise ratio. Various molecular acceptors including 6,7-diphenyl-[1,2,5]thiadiazolo[3,4-g]quinoxaline and benzobisthiadiazole (BBTD) are applied in the structure broadly [73].

BBTD is one of the electron deficient segments, which has been widely exploited as an important building part for donor-acceptor-donor (D-A-D) configuration [74]. Recently, Ma's group introduced the Se and amino groups into the BBTD skeleton, which could shift the maximal wavelength in the NIR-II window to more than 1200nm (Figure 7A–C) [75]. In this way, prepared FM1210 in this study could be utilized to detect tumors and their vasculature in mice with high resolution and signal-to-background. In addition, Dai and co-workers synthesized a BBTD-based NIR-II organic dye p-FE by constructing the shielding unit-donor-acceptor-donor-shielding unit structure (Figure 7D–F) [43].The introduction of shielding unit into the molecular skeleton reduced intermolecular interaction, which improved fluorescence QYs further. This novel NIR-II organic dye exhibited high resolution and SNR both in vitro and in vivo, which guided brain vessels imaging in mice well. Later, Tang et al. synthesized an AIE gen while BBTD as an acceptor, which could accumulate in the mucosa and submucosa layers and detect the degree of inflammatory bowel diseases [73]. Furthermore, Tang group also developed a novel AIE dye based on BBTD core and a method of "backbone distortion and molecular rotor." The fluorophores' tail emission extended to 1590 nm and maximal absorption was located at 710 nm [76]. This kind of AIEgen with brain-targeting ApoE could be utilized in NIR-IIb orthotopic glioblastoma imaging. The study showed that AIEgen based on BBTD exhibited remarkable advantages in brain blood vessel imaging and lymph node imaging, could be applied in clinical surgery and therapy.

Dipyrromethene Boron Difluoride (BODIPY) Fluorophores

BODIPY-derived structure is a kind of D-A-D configuration, which is endowed with excellent fluorescent QYs and chemical stability in water [77]. Recently, many researchers introduced nitrogen atoms into the BODIPY skeleton to form aza-BODIPY, which allowed this compound with red-shift absorption and emission wavelength together [78]. Then, Huang and his colleagues developed a series of synthesis methods to acquire a class of D-A-D based and tunable photophysical aza-BODIPY derivatives (NJ960, NJ1030, and NJ1060) (Figure 8A–C) [79]. Thanks to the electron-deficient properties of aza-BODIPY, researchers could bind it to the electron-donating groups such as 4-anisoly groups, forming the typical D-A-D structure. With the help of the intramolecular charge transfer effect of the D-A-D structure, a large emission peak red-shift to the NIR-II window could be observed. J-aggregates are well-known for their red-shifted absorption and increased fluorescence QYs and enhanced photoluminance properties, which play a vital role in constructing of

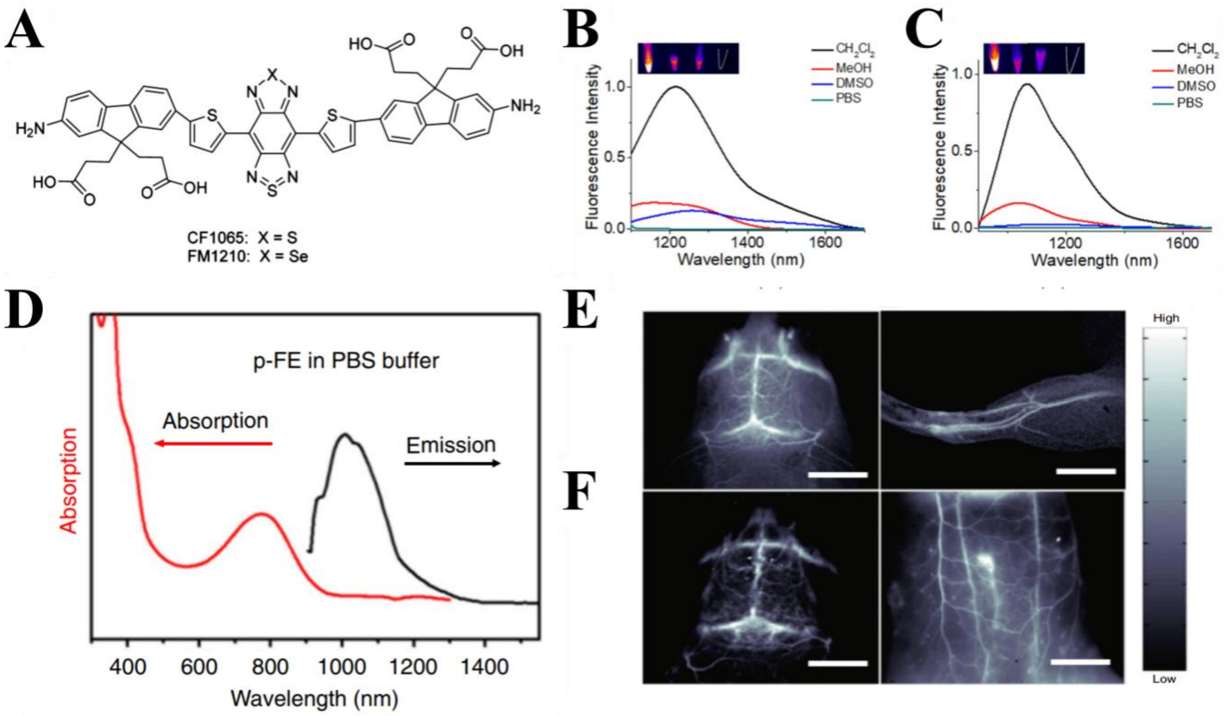

Figure 7 (A) Structures of NIR-II Fluorophores FM1210 and CF1065 (Control). Fluorescence spectra of (B) FM1210 and (C) CF1065 under the excitation of 980 and 808 nm, respectively. Insets (from left to right: CH_2Cl_2, MeOH, DMSO, PBS) are NIR-II fluorescence images of FM1210 and CF1065 with exposure time of 20 ms, respectively. Reproduced with permission. Fang Y, Shang J, Liu D, et al. Design, Synthesis, and Application of a Small Molecular NIR-II Fluorophore with Maximal Emission beyond 1200 nm. *J Am Chem Soc* 2020;142(36):15271–15275. Copyright 2020, American Chemical Society. (D) Absorption and emission spectra (excited by an 808 nm laser) of p-FE in PBS buffer. (E, F) High-magnification fluorescence imaging of brain, hindlimb, and belly of the mouse through collection of fluorescence emitting above 1100 nm with low exposure time of 2 ms (E) and above 1300 nm with exposure time of 20 ms (F). Reproduced with permission. Wan H, Yue J, Zhu S, et al. A bright organic NIR-II nanofluorophore for three-dimensional imaging into biological tissues. *Nat Commun* 2018;9(1):1171. Copyright 2018, Springer Nature. NIR-II, Near-Infrared-II.

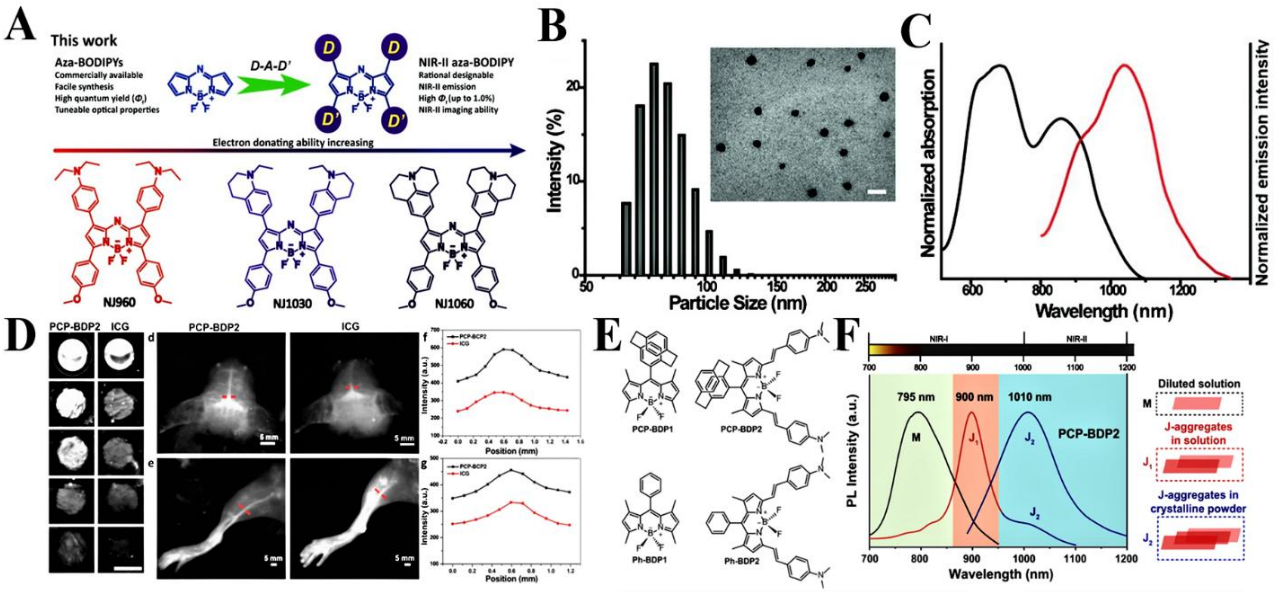

Figure 8 (A) Fluorescence maxima of selected NIR-II dyes and chemical structures of polymethines, BBTDs, NJ960, NJ1030, and NJ1060. (B) Particle size distribution of NJ1060 NPs measured by dynamic light scattering with a mean diameter of 90 nm and a PDI of 0.137. Inset: TEM images of NJ1060 NPs. (C) Normalized absorption and emission spectra of NJ1060 NPs in PBS solution. Reproduced with permission. Bai L, Sun P, Liu Y, et al. Novel aza-BODIPY based small molecular NIR-II fluorophores for in vivo imaging. *Chem Commun* 2019;55(73):10920–10923. Copyright 2019, Royal Society of Chemistry. (D) NIR-II fluorescence imaging of blood vessels in brain and hindlimb of PCP-BDP2 NPs and ICG, respectively. The quantification of fluorescent signals at the cross-section in hindlimb and brain (along the red-dashed line), respectively. The results are representative of three independent experiments. (E) Chemical structures of PCP-BDP1, PCP-BDP2, Ph-BDP1, and Ph-BDP2. (F) Fluorescence spectra of PCP-BDP2 in diluted dichloromethane solution (10 μM) (black line, "M" refers to monomer), THF-water binary solvents (10 μM, 1:9, v/v) (red line, J1-band), and the crystalline powder (blue line, J2-band). Reproduced with permission. Li K, Duan X, Jiang Z, et al. J-aggregates of meso-[2.2]paracyclophanyl-BODIPY dye for NIR-II imaging. *Nat Commun* 2021;12(1):2376. Copyright 2021, Springer Nature. NIR-II, Near-Infrared-II; BBTD, benzobisthiadiazole; PCP, paracyclophane.

organic fluorescent molecules. To date, there are many reports concerning BODIPY-derivatives J-aggregates, the question of aggregation-caused emission quenching is still challenging. Liu and coworkers reported BODIPY-based J-aggregates by introducing paracyclophane (PCP) group to the meso-position of BODIPY (Figure 8D–F) [80]. The formed PCP-BDP2 compound showed both NIR-I and NIR-II emission peaks when in its aggregation state. However, it exhibited only NIR-II emission when in its crystalline state. PCP-BDP2 could also show excellent NIR-II imaging properties. In this study, the PCP-BDP2 was utilized to image the cerebral vasculature and hindlimb vessel. Only after 5 minutes of injection, the blood vessels could be visualized in the fluorescence picture. Recently, Liu et al. reported a fluorescent probe based on BODIPY that could be activated by H_2S in vivo [81]. The emission of these series of nanoprobes' emission peaks located from 925 to 1205 nm because of the π-conjugated skeleton and enhanced electron-donating ability. By introducing a donor group into the BODIPY, the emission wavelength region was further lengthened to 1205 nm. In addition, 4-nitrothiophenol was introduced to the BODIPY scaffold, which acted as the fluorescence quencher and could be recognized by H_2S through a nucleophilic substitution reaction and turned on the NIR-II FL. With the help of specific recognition of H_2S, the formed WH-3 could be applied in the H_2S-abundant tumor site. The BODIPY-based nanoprobes could detect the fluctuation of endogenous H_2S in tumors, which could be further used to verify the relationship between H_2S fluctuation level and tumor proliferation stage.

Cyanine Dyes

Compared with D-A-D fluorophores, methylene bonds connecting two indoleamine groups formed the typical cyanine structure, which is easy to synthesize [82]. However, cyanine molecules are limited due to their chemical instability and high concentration-induced quenching problem [83]. The mechanism of distorted intramolecular charge transfer contributes to the fluorescence of cyanine dyes. ICG as one of the typical NIR-I cyanine molecules, has been approved by FDA for clinical applications. Many researchers have discovered that ICG had a tail emission in the NIR-II window [15]. Which means ICG and its derivates such as IR-820, IRDye800CW and IR-783 have potential in NIR-II FL imaging [83–85]. Hong et al. reported a NIR-II cyanine derivate by substituting oxygen atom for sulfur atom on the polymethine skeleton, whose emission wavelength is located at ~1125 nm and extended to 1400 nm (Figure 9A–C) [86]. Cyanine dyes show bright NIR-II FL during the detection of main vessels in the abdomen of C57BL/6J mice. To solve chemical instability and worse water-solubility, Zhang and co-workers developed a series of stable, high QYs and anti-solvent quenching cyanine fluorophores, which an emission wavelength could up to 1008 nm (Figure 9D–F) [87]. What's most interesting is that with the introduction of the carboxylic acid group, the cyanine fluorophores could achieve activatable NIR-II FL through spirocyclization reaction. In the study, the cyanine nanoprobes show real-time monitoring of ATP levels in the drug-induced liver injury's Kunming mouse model. Furthermore, J-Aggregates of cyanine dyes were reported by Zhang's group, which could emit NIR-II FL beyond 1300 nm in the diagnosis of blood disease (Figure 9G–I) [88]. The mouse carotid artery could be observed to expand from 370 to 680 um under the monitoring of NIR-II FL imaging.

Semiconducting polymer nanoparticles (SPNs)

Compared with other organic molecules, SPNs are composed of multiple hydrophobic π-conjugated semiconducting polymer backbones and amphiphilic monomer matrix, which the building-block monomers for polymerization determined the SPNs' bandgaps [89]. What's more, SPNs' optical properties are independent of their size and morphology [90]. Recently, Pu and co-workers developed a dual peak absorption nanoprobe, which is composed of a

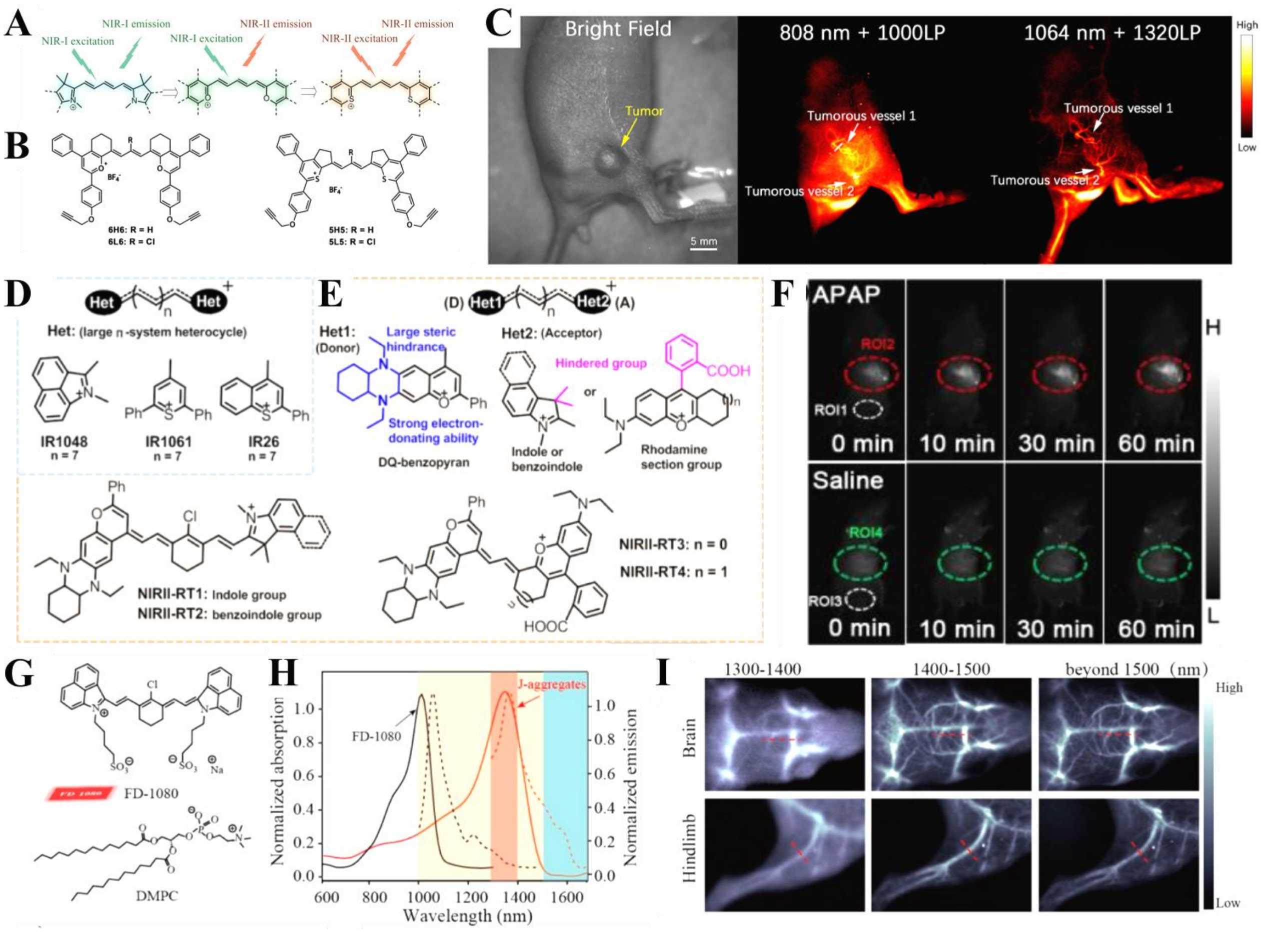

Figure 9 (A) Design strategy of small-molecule fluorophores with both excitation and emission in the NIR-II window. (B) Chemical structures of 5L5, 5H5, 6L6, and 6H6. (C) NIR-II and NIR-IIa imaging of blood vessels around and within the nude mouse tumors under ~100 mW cm^{-2} 808 nm laser irradiation and 1000LP filter (middle, 100 ms exposure time), or ~100 mW cm^{-2} 1064 nm laser irradiation and 1320LP filter (right, 500 ms exposure time). Reproduced with permission. Ding B, Xiao Y, Zhou H, et al. Polymethine Thiopyrylium Fluorophores with Absorption beyond 1000 nm for Biological Imaging in the Second Near-Infrared Subwindow. *J Med Chem* 2018;62(4):2049–2059. Copyright 2018, American Chemical Society. (D) Structure of the reported NIR-II cyanines. (E) Rational design of the novel NIR-II cyanine fluorophores NIRII-RT1-4. (F) Real-time images of NIRII-RT-ATP in livers of mouse simulated with saline or APAP (300 mg/kg) at different time points. Reproduced with permission.Ren T, Wang Z, Xiang Z, et al. A General Strategy for Development of Activatable NIR‐II Fluorescent Probes for In Vivo High‐Contrast Bioimaging. *Angew Chem Int Ed* 2020;60(2):800–805. Copyright 2021, Wiley-VCH. (G) Structure of FD-1080 and DMPC. (H) Normalized absorption (solid lines) and emission (dashed line) of FD-1080 monomer and J-aggregates. (I) Images of brain and hindlimb vessels achieved by J-aggregates in varied regions. Reproduced with permission. Sun C, Li B, Zhao M, et al. J-Aggregates of Cyanine Dye for NIR-II in Vivo Dynamic Vascular Imaging beyond 1500 nm. J Am Chem Soc 2019;141(49):19221–19225. Copyright 2019, American Chemical Society. NIR-II, Near-Infrared-II; NIR-IIa, Near-Infrared IIa.

semiconducting copolymer including two parts exhibiting absorption both in NIR-I and NIR-II biological windows, respectively (Figure 10A–C) [91]. These SPNs could be utilized for deep-tissue tumor NIR-II PTT and provide an opportunity to compare results between NIR-I PTT and NIR-II PTT. Furthermore, Fan and his colleagues fabricated a SPNs-based nanoprobe for NIR-II imaging-guided PTT/thermodynamic therapy combination therapy (Figure 10D–F) [92]. The compound is synthesized by encapsulating a NIR-II fluorescent SP molecule into an amphiphilic copolymer, then loading up the SPN with an azo compound, 2,2’-azobis[2-(2-imidazolin-2-yl)propane] dihydrochloride via an electrostatic reaction. After injection of this compound into tumor-bearing mice model, the tumor can be visualized under NIR-II FL. However, due to the strong intermolecular π-πstacking interaction, the emissions of aggregated SPNs are frequently quenched. Tang et al. designed enhanced brightness NIR-II SPNs with structure planarization and twisting [93]. While the planar segment assured high absorption efficiency and the twisted segment ensured high photoluminescence QYs. Fabricated pNIR-4 NPs showed an emission peak at 1040 nm and the tail emission extended to NIR-IIa biological window. The SPNs nanoprobe could verify the distribution in blood vessels of the mouse brain and hindlimb with increased SBR and high resolution. In addition, the pNIR-4 NPs could also be utilized to instruct tumor surgery resection and guide intraoperative resection plans.

Conclusion and outlook

Over the past decades, we have witnessed remarkable progress in biological imaging in the NIR-II window. Lower extinction coefficients of biological tissues in the NIR-II window enable reduced photon scattering and diminished tissue autofluorescence. NIR-II FLI with unparalleled spatial and temporal resolution requires investigation of multifunctional and efficient nanoprobes (inorganic/organic nanoprobes). Therefore, the NIR-II fluorescent nanoprobes could establish pathological association between biological and molecular level. Many strategies have been explored for the synthesis and modification of exogenous nanoprobes with NIR-II absorption and emission.

Herein, we summarized recent progress in versatile types of inorganic/organic nanoprobes, including their species, advantages and applications.

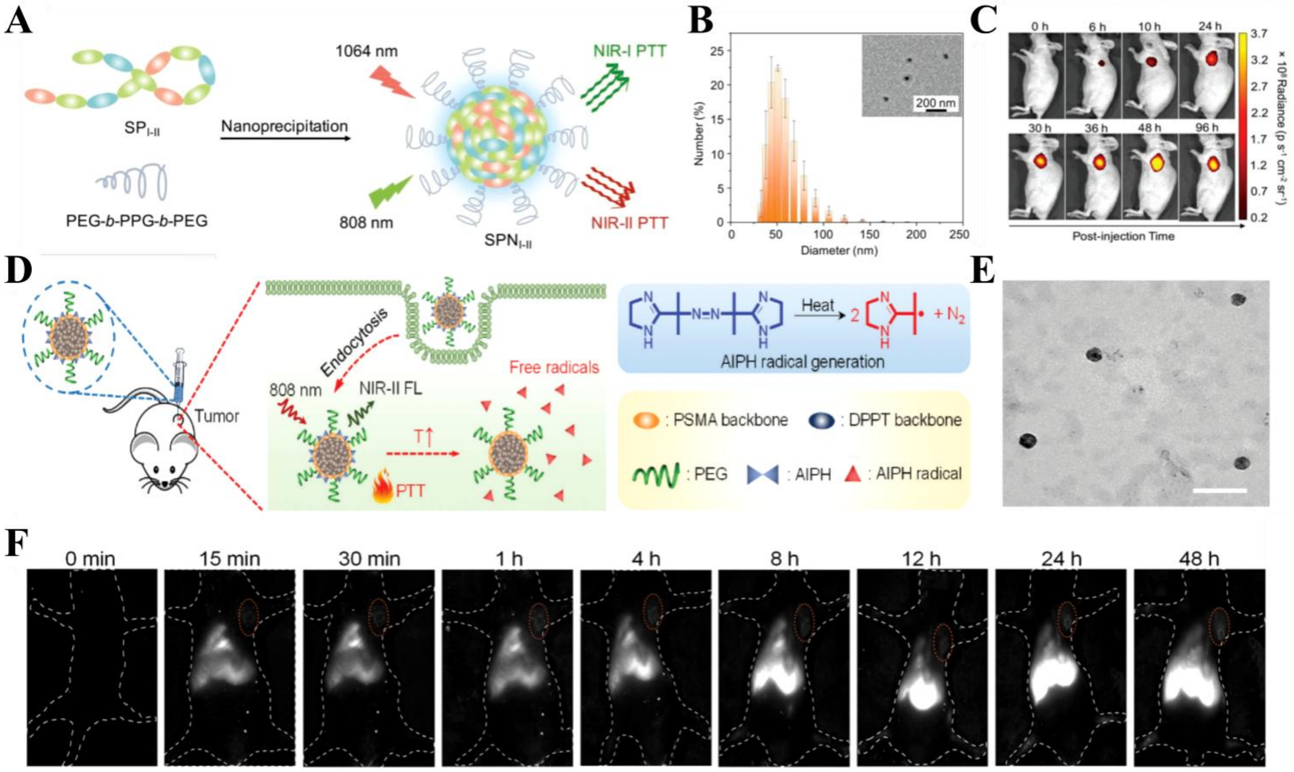

Figure 10 (A) Schematic illustration of SPNFI-II. (B) DLS profile of SPNI-IIs in 1 × PBS. Error bars indicated standard deviations of three separate measurements. Inset: Representative TEM image of SPNI-IIs. (C) Fluorescence images of living mice bearing xenograft 4T1 tumors at 0, 6, 10, 24, 30, 36, 48, and 96 h after systemic administration of SPNFI-II through tail-vein injection (200 μL, SPI-II 200 μg mL^{-1}). All the fluorescence data were collected with excitation and emission at 710 and 780 nm, respectively. Reproduced with permission. Jiang Y, Li J, Zhen X, et al. Dual-Peak Absorbing Semiconducting Copolymer Nanoparticles for First and Second Near-Infrared Window Photothermal Therapy: A Comparative Study. *Adv Mater* 2018;30(14):e:1705980. Copyright 2018, Wiley-VCH (D) Schematic illustration for the in vivo NIR-II fluorescence imaging-guided thermodynamic therapy of ADPPTN. (E) Representative TEM image of ADPPTN. The scale bar represents 100 nm. (F) Representative NIR-II fluorescence images of tumor-bearing mice at different time points after i.v. injection of ADPPTN (200 μg mL^{-1}, 200 μL). The tumor regions are marked with red circles. Reproduced with permission. Wang W, Zhang X, Ni X, et al. Semiconducting polymer nanoparticles for NIR-II fluorescence imaging-guided photothermal/thermodynamic combination therapy. *Biomater Sci* 2022;10(3):846–853. Copyright 2021, Royal Society of Chemistry. NIR-II, Near-Infrared-II.

Considering numerous advantages of inorganic/organic nanoprobes, they have exhibited great potential in biomedical applications. Firstly, the biocompatibility of nanoprobes plays an important role in preclinical and clinical applications. For instance, the existence of heavy-metal ions such as Pb2$^+$, Hg2$^+$, Cd2$^+$, and As3$^-$ result in long-term potential toxicity. To overcome this problem, the surface modification layer possessed charge and functional groups can largely determine the fate and toxicity of the nanoprobes in vivo. Besides that, the surface modification layer cannot be too thick to meet the renal clearance requirement ($<$5.5nm). Hence, it is of great importance to construct biodegradable and size-controllable nanoprobes for NIR-II biomedical applications. Taking advantage of the biocompatible nanoprobes, NIR-II FLI could be utilized to detect anatomical structures accurately and safely (vascular imaging, lymphatic detection and skeleton imaging), which could discriminate anatomical structures with higher resolution and deeper penetration depth.

Secondly, stability and effective accumulation in lesions are always key factors before clinical translation. Most small-molecule organic fluorophores could be easily metabolized from body before they reach the lesions compared to inorganic nanoprobes. In addition, many organic fluorophores with high molecular weight are restricted by poor stability in physiological conditions, which always results in severe fluorescence quenching. Strategies to acquire stable fluorophores structurally should be further explored. Remarkably, constructing activable organic fluorophores are highly required in NIR-II FLI. In response to pH, redox conditions and biomolecules, the activable NIR-II FLI nanoprobes can distinguish and visualize disease area from normal structures. Reactive oxygen species and nitrogen species-activable nanoprobes could be turned-on in specific pathogenic conditions and visualize disease sites such as colorectal cancers, rheumatoid arthritis and neurodegenerative disorders. Biological environment is highly complicated that constituted of many reactive species. Thus, efforts should be taken to improve a series of nanoprobes that can respond to different substances and present differentiable signals in NIR-II FLI.

Thirdly, only a few nanoprobes' emission peaks can extend to the NIR-IIb window. At present, most NIR-II organic/inorganic nanoprobes are located in the range of 1000–1200 nm due to complicated molecular design. Higher SNR and lower tissue auto-fluorescence could be acquired by NIR-IIb FLI. Hence more efforts should be made to optimize design strategy and further structural modification to expand the emission spectrum range. Based on NIR-II FLI, image-guided surgery and therapy can be carried out in a non-radiative strategy. Image-guided surgery is conductive to resect lymph nodes and outline the target tissue accurately, that can be applied into clinical human surgery in the future.

In conclusion, organic and inorganic nanoprobes hold great promise in the NIR-II FLI. Each class of nanoprobes has its unique photophysical and chemical properties, the combination of inorganic and organic nanoprobes will have more excellent characteristics. Numerous novel nanoprobes have been investigated in recent years, however, the biocompatible and high fluorescent QYs nanoprobes that can be applied to clinical practice still have a long way to go.

References

1. Manafi-Farid R, Askari E, Shiri I, et al. [18F]FDG-PET/CT Radiomics and Artificial Intelligence in Lung Cancer: Technical Aspects and Potential Clinical Applications. *Seminars in Nuclear Medicine* 2022;52(6):759–780. Available at: http://dx.doi.org/10.1053/j.semnuclmed.2022.04.004
2. Lustig M, Donoho D, Pauly JM. Sparse MRI: The application of compressed sensing for rapid MR imaging. *Magn Reson Med* 2007;58(6):1182–1195. Available at: http://dx.doi.org/10.1002/mrm.21391
3. Fields BKK, Demirjian NL, Dadgar H, et al. Imaging of COVID-19: CT, MRI, and PET. *Seminars in Nuclear Medicine* 2021;51(4):312–320. Available at: http://dx.doi.org/10.1053/j.semnuclmed.2020.11.003
4. Anttinen M, Ettala O, Malaspina S, et al. A Prospective Comparison of 18F-prostate-specific Membrane Antigen-1007 Positron Emission Tomography Computed Tomography, Whole-body 1.5 T Magnetic Resonance Imaging with Diffusion-weighted Imaging, and Single-photon Emission Computed Tomography/Computed Tomography with Traditional Imaging in Primary Distant Metastasis Staging of Prostate Cancer (PROSTAGE). *European Urology Oncology* 2021;4(4):635–644. Available at: http://dx.doi.org/10.1016/j.euo.2020.06.012
5. Buckner RL, Krienen FM, Yeo BTT. Opportunities and limitations of intrinsic functional connectivity MRI. *Nat Neurosci* 2013;16(7):832–837. Available at: http://dx.doi.org/10.1038/nn.3423
6. Jiang Y, Pu K. Molecular Probes for Autofluorescence-Free Optical Imaging. *Chem Rev* 2021;121(21):13086–13131. Available at: http://dx.doi.org/10.1021/acs.chemrev.1c00506
7. Martin KE, Cosby AG, Boros E. Multiplex and In Vivo Optical Imaging of Discrete Luminescent Lanthanide Complexes Enabled by In Situ Cherenkov Radiation Mediated Energy Transfer. *J Am Chem Soc* 2021;143(24):9206–9214. Available at: http://dx.doi.org/10.1021/jacs.1c04264
8. Brindle K. New approaches for imaging tumour responses to treatment. *Nat Rev Cancer* 2008;8(2):94–107. Available at: http://dx.doi.org/10.1038/nrc2289
9. Pacheco PE, Hill SM, Henriques SM, et al. The novel use of intraoperative laser-induced fluorescence of indocyanine green tissue angiography for evaluation of the gastric conduit in esophageal reconstructive surgery. *The American Journal of Surgery* 2013;205(3):349–353. Available at: http://dx.doi.org/10.1016/j.amjsurg.2012.11.005
10. Yoon S, Kim M, Jang M, et al. Deep optical imaging within complex scattering media. *Nat Rev Phys* 2020;2(3):141–158. Available at: http://dx.doi.org/10.1038/s42254-019-0143-2
11. Schneider SL, Kohli I, Hamzavi IH, et al. Emerging imaging technologies in dermatology. *Journal of the American Academy of Dermatology* 2019;80(4):1121–1131. Available at: http://dx.doi.org/10.1016/j.jaad.2018.11.043
12. Li C, Wang Q. Challenges and Opportunities for Intravital Near-Infrared Fluorescence Imaging Technology in the Second Transparency Window. *ACS Nano* 2018;12(10):9654–9659. Available at: http://dx.doi.org/10.1021/acsnano.8b07536
13. Manley M. Near-infrared spectroscopy and hyperspectral imaging: non-destructive analysis of biological materials. *Chem Soc Rev* 2014;43(24):8200–8214. Available at: http://dx.doi.org/10.1039/C4CS00062E
14. Hong G, Antaris AL, Dai H. Near-infrared fluorophores for biomedical imaging. *Nat Biomed Eng* 2017;1(1):0010. Available at: http://dx.doi.org/10.1038/s41551-016-0010
15. Ma R, Alifu N, Du Z, et al. Indocyanine Green-Based Theranostic Nanoplatform for NIR Fluorescence Image-Guided Chemo/Photothermal Therapy of Cervical Cancer. *IJN* 2021;16:4847–4861. Available at: http://dx.doi.org/10.2147/IJN.S318678
16. Wang S, Liu J, Feng G, et al. NIR-II Excitable Conjugated Polymer Dots with Bright NIR-I Emission for Deep In Vivo Two-Photon Brain Imaging Through Intact Skull. *Adv Funct Mater* 2019;29(15):1808365. Available at: http://dx.doi.org/10.1002/adfm.201808365
17. Sajedi S, Sabet H, Choi HS. Intraoperative biophotonic imaging systems for image-guided interventions. *Nanophotonics* 2018;8(1):99–116. Available at: http://dx.doi.org/10.1515/nanoph-2018-0134
18. Matsui A, Tanaka E, Choi HS, et al. Real-time intra-operative near-infrared fluorescence identification of the extrahepatic bile ducts using clinically available contrast agents. *Surgery* 2010;148(1):87–95. Available at: http://dx.doi.org/10.1016/j.surg.2009.12.004
19. Ashitate Y, Vooght CS, Hutteman M, et al. Simultaneous Assessment of Luminal Integrity and Vascular Perfusion of the Gastrointestinal Tract Using Dual-Channel Near-Infrared Fluorescence. *Mol Imaging* 2012;11(4):7290.2011.00048. Available at: http://dx.doi.org/10.2310/7290.2011.00048
20. Troyan SL, Kianzad V, Gibbs-Strauss SL, et al. The FLARE™ Intraoperative Near-Infrared Fluorescence Imaging System: A First-in-Human Clinical Trial in Breast Cancer Sentinel Lymph Node Mapping. *Ann Surg Oncol* 2009;16(10):2943–2952. Available at: http://dx.doi.org/10.1245/s10434-009-0594-2
21. Verbeek FPR, van der Vorst JR, Schaafsma BE, et al. Intraoperative Near Infrared Fluorescence Guided Identification of the Ureters Using Low Dose Methylene Blue: A First in Human Experience. *Journal of Urology* 2013;190(2):574–579. Available at: http://dx.doi.org/10.1016/j.juro.2013.02.3187
22. Tsukasaki Y, Komatsuzaki A, Mori Y, et al. A short-wavelength infrared emitting multimodal probe for non-invasive visualization of phagocyte cell migration in living mice. *Chem Commun* 2014;50(92):14356–14359. Available at: http://dx.doi.org/10.1039/C4CC06542E
23. Li B, Lu L, Zhao M, et al. An Efficient 1064 nm NIR-II Excitation Fluorescent Molecular Dye for Deep-Tissue High-Resolution Dynamic Bioimaging. *Angew Chem Int Ed* 2018;57(25):7483–7487. Available at: http://dx.doi.org/10.1002/anie.201801226
24. Hong G, Diao S, Antaris AL, et al. Carbon Nanomaterials for Biological Imaging and Nanomedicinal Therapy. *Chem Rev* 2015;115(19):10816–10906. Available at: http://dx.doi.org/10.1021/acs.chemrev.5b00008
25. Diao S, Hong G, Antaris AL, et al. Biological imaging without autofluorescence in the second near-infrared region. *Nano Res* 2015;8(9):3027–3034. Available at: http://dx.doi.org/10.1007/s12274-015-0808-9
26. Mi C, Guan M, Zhang X, et al. High Spatial and Temporal Resolution NIR-IIb Gastrointestinal Imaging in Mice. *Nano Lett* 2022;22(7):2793–2800. Available at: http://dx.doi.org/10.1021/acs.nanolett.1c04909
27. Lei Z, Zhang F. Molecular Engineering of NIR-II Fluorophores for Improved Biomedical Detection. *Angew Chem Int Ed* 2021;60(30):16294–16308. Available at: http://dx.doi.org/10.1002/anie.202007040
28. Wang P, Fan Y, Lu L, et al. NIR-II nanoprobes in-vivo assembly to improve image-guided surgery for metastatic ovarian cancer. *Nat Commun* 2018;9(1). Available at: http://dx.doi.org/10.1038/s41467-018-05113-8
29. Ge X, Su L, Yang L, et al. NIR-II Fluorescent Biodegradable Nanoprobes for Precise Acute Kidney/Liver Injury Imaging and Therapy. *Anal Chem* 2021;93(41):13893–13903. Available at:

http://dx.doi.org/10.1021/acs.analchem.1c02742

30. Welsher K, Liu Z, Sherlock SP, et al. A route to brightly fluorescent carbon nanotubes for near-infrared imaging in mice. *Nature Nanotech* 2009;4(11):773–780. Available at: http://dx.doi.org/10.1038/nnano.2009.294
31. Hu Z, Fang C, Li B, et al. First-in-human liver-tumour surgery guided by multispectral fluorescence imaging in the visible and near-infrared-I/II windows. *Nat Biomed Eng* 2019;4(3):259–271. Available at: http://dx.doi.org/10.1038/s41551-019-0494-0
32. Yang J, He S, Hu Z, et al. In vivo multifunctional fluorescence imaging using liposome-coated lanthanide nanoparticles in near-infrared-II/IIa/IIb windows. *Nano Today* 2021;38:101120. Available at: http://dx.doi.org/10.1016/j.nantod.2021.101120
33. Dou K, Huang W, Xiang Y, et al. Design of Activatable NIR-II Molecular Probe for In Vivo Elucidation of Disease-Related Viscosity Variations. *Anal Chem* 2020;92(6):4177–4181. Available at: http://dx.doi.org/10.1021/acs.analchem.0c00634
34. Chen P, Chen X, Hepfer RG, et al. A noninvasive fluorescence imaging-based platform measures 3D anisotropic extracellular diffusion. *Nat Commun* 2021;12(1):1913. Available at: http://dx.doi.org/10.1038/s41467-021-22221-0
35. Zeng X, Xie L, Chen D, et al. A bright NIR-II fluorescent probe for breast carcinoma imaging and image-guided surgery. *Chem Commun* 2019;55(95):14287–14290. Available at: http://dx.doi.org/10.1039/C9CC07694H
36. Yao D, Wang Y, Zou R, et al. Molecular Engineered Squaraine Nanoprobe for NIR-II/Photoacoustic Imaging and Photothermal Therapy of Metastatic Breast Cancer. *ACS Appl Mater Interfaces* 2020;12(4):4276–4284. Available at: http://dx.doi.org/10.1021/acsami.9b20147
37. Chen J, Chen L, Wu Y, et al. A H2O2-activatable nanoprobe for diagnosing interstitial cystitis and liver ischemia-reperfusion injury via multispectral optoacoustic tomography and NIR-II fluorescent imaging. *Nat Commun* 2021;12(1):6870. Available at: http://dx.doi.org/10.1038/s41467-021-27233-4
38. Mandal AK, Wu X, Ferreira JS, et al. Fluorescent sp3 Defect-Tailored Carbon Nanotubes Enable NIR-II Single Particle Imaging in Live Brain Slices at Ultra-Low Excitation Doses. *Sci Rep* 2020;10(1):5286. Available at: http://dx.doi.org/10.1038/s41598-020-62201-w
39. Takeuchi T, Iizumi Y, Yudasaka M, et al. Characterization and Biodistribution Analysis of Oxygen-Doped Single-Walled Carbon Nanotubes Used as in Vivo Fluorescence Imaging Probes. *Bioconjugate Chem* 2019;30(5):1323–1330. Available at: http://dx.doi.org/10.1021/acs.bioconjchem.9b00088
40. Tian H, Lin J, Zhu F, et al. 2D graphene oxide-L-arginine-soybean lecithin nanogenerator for synergistic photothermal and NO gas therapy. *Chinese Chemical Letters* 2022. Available at: http://dx.doi.org/10.1016/j.cclet.2022.05.091
41. Li Y, Bai G, Zeng S, et al. Theranostic Carbon Dots with Innovative NIR-II Emission for in Vivo Renal-Excreted Optical Imaging and Photothermal Therapy. *ACS Appl Mater Interfaces* 2019;11(5):4737–4744. Available at: http://dx.doi.org/10.1021/acsami.8b14877
42. Han Y, Liu H, Fan M, et al. Near-infrared-II photothermal ultra-small carbon dots promoting anticancer efficiency by enhancing tumor penetration. *J Colloid Interface Sci* 2022;616:595–604. Available at: http://dx.doi.org/10.1016/j.jcis.2022.02.083
43. Wan H, Yue J, Zhu S, et al. A bright organic NIR-II nanofluorophore for three-dimensional imaging into biological tissues. *Nat Commun* 2018;9(1):1171. Available at: http://dx.doi.org/10.1038/s41467-018-03505-4
44. Hong G, Lee JC, Robinson JT, et al. Multifunctional in vivo vascular imaging using near-infrared II fluorescence. *Nat Med* 2012;18(12):1841–1846. Available at: http://dx.doi.org/10.1038/nm.2995
45. Bardhan NM, Ghosh D, Belcher AM. Carbon nanotubes as in vivo bacterial probes. *Nat Commun* 2014;5:4918. Available at: http://dx.doi.org/10.1038/ncomms5918
46. Liang C, Diao S, Wang C, et al. Tumor Metastasis Inhibition by Imaging-Guided Photothermal Therapy with Single-Walled Carbon Nanotubes. *Adv Mater* 2014;26(32):5646–5652. Available at: http://dx.doi.org/10.1002/adma.201401825
47. Ceppi L, Bardhan NM, Na Y, et al. Real-Time Single-Walled Carbon Nanotube-Based Fluorescence Imaging Improves Survival after Debulking Surgery in an Ovarian Cancer Model. *ACS Nano* 2019;13(5):5356–5365. Available at: http://dx.doi.org/10.1021/acsnano.8b09829
48. Iverson NM, Barone PW, Shandell M, et al. In vivo biosensing via tissue-localizable near-infrared-fluorescent single-walled carbon nanotubes. *Nature Nanotech* 2013;8(11):873–880. Available at: http://dx.doi.org/10.1038/nnano.2013.222
49. Jin H, Heller DA, Kalbacova M, et al. Detection of single-molecule H2O2 signalling from epidermal growth factor receptor using fluorescent single-walled carbon nanotubes. *Nature Nanotech* 2010;5(4):302–309. Available at: http://dx.doi.org/10.1038/nnano.2010.24
50. Diao S, Blackburn JL, Hong G, et al. Fluorescence Imaging In Vivo at Wavelengths beyond 1500 nm. *Angew Chem Int Ed* 2015;54(49):14758–14762. Available at: http://dx.doi.org/10.1002/anie.201507473
51. Zhang H, Sun C, Sun L, et al. Stable Monodisperse Pb1-x Cdx S Quantum Dots for NIR-II Bioimaging by Aqueous Coprecipitation of Bimetallic Clusters. *Angew Chem Int Ed Engl* 2022;61(37):e202203851. https://dx.doi.org/10.1002/anie.202203851
52. Li Y, Zhang P, Tang W, et al. Bright, Magnetic NIR-II Quantum Dot Probe for Sensitive Dual-Modality Imaging and Intensive Combination Therapy of Cancer. *ACS Nano* 2022;16(5):8076–8094. Available at: http://dx.doi.org/10.1021/acsnano.2c01153
53. Wang P, Li J, Wei M, et al. Tumor-microenvironment triggered signal-to-noise boosting nanoprobes for NIR-IIb fluorescence imaging guided tumor surgery and NIR-II photothermal therapy. *Biomaterials* 2022;287:121636. Available at: http://dx.doi.org/10.1016/j.biomaterials.2022.121636
54. Chen G, Tian F, Zhang Y, et al. Tracking of Transplanted Human Mesenchymal Stem Cells in Living Mice using Near-Infrared Ag2S Quantum Dots. *Adv Funct Mater* 2013;24(17):2481–2488. Available at: http://dx.doi.org/10.1002/adfm.201303263
55. Hong G, Robinson JT, Zhang Y, et al. In Vivo Fluorescence Imaging with Ag2S Quantum Dots in the Second Near-Infrared Region. *Angew Chem Int Ed* 2012;51(39):9818–9821. Available at: http://dx.doi.org/10.1002/anie.201206059
56. Zheng Z, Dai R, Jia Z, et al. Biodegradable Multifunctional Nanotheranostic Based on Ag2S-Doped Hollow BSA-SiO2 for Enhancing ROS-Feedback Synergistic Antitumor Therapy. *ACS Appl Mater Interfaces* 2020;12(49):54356–54366. Available at: http://dx.doi.org/10.1021/acsami.0c14855
57. Dong B, Li C, Chen G, et al. Facile Synthesis of Highly Photoluminescent Ag2Se Quantum Dots as a New Fluorescent Probe in the Second Near-Infrared Window for in Vivo Imaging. *Chem Mater* 2013;25(12):2503–2509. Available at: http://dx.doi.org/10.1021/cm400812v
58. Yang H, Li R, Zhang Y, et al. Colloidal Alloyed Quantum Dots with Enhanced Photoluminescence Quantum Yield in the NIR-II Window. *J Am Chem Soc* 2021;143(6):2601–2607. Available at: http://dx.doi.org/10.1021/jacs.0c13071

59. Ling S, Yang X, Li C, et al. Tumor Microenvironment-Activated NIR-II Nanotheranostic System for Precise Diagnosis and Treatment of Peritoneal Metastasis. *Angew Chem Int Ed* 2020;59(18):7219–7223. Available at: http://dx.doi.org/10.1002/anie.202000947
60. Wang F, Ren F, Ma Z, et al. In vivo non-invasive confocal fluorescence imaging beyond 1,700 nm using superconducting nanowire single-photon detectors. *Nat Nanotechnol* 2022;17(6):653–660. Available at: http://dx.doi.org/10.1038/s41565-022-01130-3
61. Du P, An R, Liang Y, et al. Emerging NIR-II luminescent bioprobes based on lanthanide-doped nanoparticles: From design towards diverse bioapplications. *Coordination Chemistry Reviews* 2022;471:214745. Available at: http://dx.doi.org/10.1016/j.ccr.2022.214745
62. Liu Z, Yun B, Han Y, et al. Dye-Sensitized Rare Earth Nanoparticles with Up/Down Conversion Luminescence for On-Demand Gas Therapy of Glioblastoma Guided by NIR-II Fluorescence Imaging. *Adv Healthcare Materials* 2021;11(3):2102042. Available at: http://dx.doi.org/10.1002/adhm.202102042
63. Naczynski DJ, Tan MC, Zevon M, et al. Rare-earth-doped biological composites as in vivo shortwave infrared reporters. *Nat Commun* 2013;4:2199. Available at: http://dx.doi.org/10.1038/ncomms3199
64. He S, Chen S, Li D, et al. High Affinity to Skeleton Rare Earth Doped Nanoparticles for Near-Infrared II Imaging. *Nano Lett* 2019;19(5):2985–2992. Available at: http://dx.doi.org/10.1021/acs.nanolett.9b00140
65. Zhong Y, Ma Z, Wang F, et al. In vivo molecular imaging for immunotherapy using ultra-bright near-infrared-IIb rare-earth nanoparticles. *Nat Biotechnol* 2019;37(11):1322–1331. Available at: http://dx.doi.org/10.1038/s41587-019-0262-4
66. Ma H, Wang J, Zhang X-D. Near-infrared II emissive metal clusters: From atom physics to biomedicine. *Coordination Chemistry Reviews* 2021;448:214184. Available at: http://dx.doi.org/10.1016/j.ccr.2021.214184
67. Yu Y, Luo Z, Yu Y, et al. Observation of Cluster Size Growth in CO-Directed Synthesis of Au25(SR)18 Nanoclusters. *ACS Nano* 2012;6(9):7920–7927. Available at: http://dx.doi.org/10.1021/nn3023206
68. Liu H, Hong G, Luo Z, et al. Atomic-Precision Gold Clusters for NIR-II Imaging. *Adv Mater* 2019;31(46):1901015. Available at: http://dx.doi.org/10.1002/adma.201901015
69. Li D, Liu Q, Qi Q, et al. Gold Nanoclusters for NIR-II Fluorescence Imaging of Bones. *Small* 2020;16(43):2003851. Available at: http://dx.doi.org/10.1002/smll.202003851
70. Chen Y, Montana DM, Wei H, et al. Shortwave Infrared in Vivo Imaging with Gold Nanoclusters. *Nano Lett* 2017;17(10):6330–6334. Available at: http://dx.doi.org/10.1021/acs.nanolett.7b03070
71. Manju CK, Ghosh D, Bodiuzzaman M, et al. Formation of an NIR-emitting Ag34S3SBB20(CF3COO)62+ cluster from a hydride-protected silver cluster. *Dalton Trans* 2019;48(24):8664–8670. Available at: http://dx.doi.org/10.1039/C9DT01533G
72. Gilroy KD, Ruditskiy A, Peng H-C, et al. Bimetallic Nanocrystals: Syntheses, Properties, and Applications. *Chem Rev* 2016;116(18):10414–10472. Available at: http://dx.doi.org/10.1021/acs.chemrev.6b00211
73. Fan X, Xia Q, Zhang Y, et al. Aggregation-Induced Emission (AIE) Nanoparticles-Assisted NIR-II Fluorescence Imaging-Guided Diagnosis and Surgery for Inflammatory Bowel Disease (IBD). *Adv Healthcare Materials* 2021;10(24):2101043. Available at: http://dx.doi.org/10.1002/adhm.202101043
74. Xu W, Wang D, Tang BZ. NIR-II AIEgens: A Win–Win Integration towards Bioapplications. *Angew Chem Int Ed* 2020;60(14):7476–7487. Available at: http://dx.doi.org/10.1002/anie.202005899
75. Fang Y, Shang J, Liu D, et al. Design, Synthesis, and Application of a Small Molecular NIR-II Fluorophore with Maximal Emission beyond 1200 nm. *J Am Chem Soc* 2020;142(36):15271–15275. Available at: http://dx.doi.org/10.1021/jacs.0c08187
76. Wang J, Liu Y, Morsch M, et al. Brain-Targeted Aggregation-Induced-Emission Nanoparticles with Near-Infrared Imaging at 1550 nm Boosts Orthotopic Glioblastoma Theranostics. *Adv Mater* 2021;34(5):e2106082. Available at: http://dx.doi.org/10.1002/adma.202106082
77. Godard A, Kalot G, Pliquett J, et al. Water-Soluble Aza-BODIPYs: Biocompatible Organic Dyes for High Contrast In Vivo NIR-II Imaging. *Bioconjugate Chem* 2020;31(4):1088–1092. Available at: http://dx.doi.org/10.1021/acs.bioconjchem.0c00175
78. Rana P, Singh N, Majumdar P, et al. Evolution of BODIPY/aza-BODIPY dyes for organic photoredox/energy transfer catalysis. *Coordination Chemistry Reviews* 2022;470:214698. Available at: http://dx.doi.org/10.1016/j.ccr.2022.214698
79. Bai L, Sun P, Liu Y, et al. Novel aza-BODIPY based small molecular NIR-II fluorophores for in vivo imaging. *Chem Commun* 2019;55(73):10920–10923. Available at: http://dx.doi.org/10.1039/C9CC03378E
80. Li K, Duan X, Jiang Z, et al. J-aggregates of meso-[2.2]paracyclophanyl-BODIPY dye for NIR-II imaging. *Nat Commun* 2021;12(1):2376. Available at: http://dx.doi.org/10.1038/s41467-021-22686-z
81. Dou K, Feng W, Fan C, et al. Flexible Designing Strategy to Construct Activatable NIR-II Fluorescent Probes with Emission Maxima beyond 1200 nm. *Anal Chem* 2021;93(8):4006–4014. Available at: http://dx.doi.org/10.1021/acs.analchem.0c04990
82. Qian H, Cheng Q, Tian Y, et al. An anti-aggregation NIR-II heptamethine-cyanine dye with a stereo-specific cyanine for imaging-guided photothermal therapy. *J Mater Chem B* 2021;9(11):2688–2696. Available at: http://dx.doi.org/10.1039/D1TB00018G
83. Chen T, Zheng Y, Gao Y, et al. Photostability investigation of a near-infrared-II heptamethine cyanine dye. *Bioorganic Chemistry* 2022;126:105903. Available at: http://dx.doi.org/10.1016/j.bioorg.2022.105903
84. Krishnan G, Berg NS van den, Nishio N, et al. Metastatic and sentinel lymph node mapping using intravenously delivered Panitumumab-IRDye800CW. *Theranostics* 2021;11(15):7188–7198. Available at: http://dx.doi.org/10.7150/thno.55389
85. Tan B, Wu Y, Wu Y, et al. Curcumin-Microsphere/IR820 Hybrid Bifunctional Hydrogels for In Situ Osteosarcoma Chemo-co-Thermal Therapy and Bone Reconstruction. *ACS Appl Mater Interfaces* 2021;13(27):31542–31553. Available at: http://dx.doi.org/10.1021/acsami.1c08775
86. Ding B, Xiao Y, Zhou H, et al. Polymethine Thiopyrylium Fluorophores with Absorption beyond 1000 nm for Biological Imaging in the Second Near-Infrared Subwindow. *J Med Chem* 2018;62(4):2049–2059. Available at: http://dx.doi.org/10.1021/acs.jmedchem.8b01682
87. Ren T, Wang Z, Xiang Z, et al. A General Strategy for Development of Activatable NIR-II Fluorescent Probes for In Vivo High-Contrast Bioimaging. *Angew Chem Int Ed* 2020;60(2):800–805. Available at: http://dx.doi.org/10.1002/anie.202009986
88. Sun C, Li B, Zhao M, et al. J-Aggregates of Cyanine Dye for NIR-II in Vivo Dynamic Vascular Imaging beyond 1500 nm. *J Am Chem Soc* 2019;141(49):19221–19225. Available at: http://dx.doi.org/10.1021/jacs.9b10043
89. Tang D, Yu Y, Zhang J, et al. Self-Sacrificially Degradable

Pseudo-Semiconducting Polymer Nanoparticles that Integrate NIR-II Fluorescence Bioimaging, Photodynamic Immunotherapy, and Photo-Activated Chemotherapy. *Adv Mater* 2022;34(34):e2203820. Available at: http://dx.doi.org/10.1002/adma.202203820

90. Zhou H, Lu Z, Zhang Y, et al. Simultaneous Enhancement of the Long-Wavelength NIR-II Brightness and Photothermal Performance of Semiconducting Polymer Nanoparticles. *ACS Appl Mater Interfaces* 2022;14(7):8705–8717. Available at: http://dx.doi.org/10.1021/acsami.1c20722
91. Jiang Y, Li J, Zhen X, et al. Dual-Peak Absorbing Semiconducting Copolymer Nanoparticles for First and Second Near-Infrared Window Photothermal Therapy: A Comparative Study. *Adv Mater* 2018;30(14):e1705980. Available at: http://dx.doi.org/10.1002/adma.201705980
92. Wang W, Zhang X, Ni X, et al. Semiconducting polymer nanoparticles for NIR-II fluorescence imaging-guided photothermal/thermodynamic combination therapy. *Biomater Sci* 2022;10(3):846–853. Available at: http://dx.doi.org/10.1039/D1BM01646F
93. Liu S, Ou H, Li Y, et al. Planar and Twisted Molecular Structure Leads to the High Brightness of Semiconducting Polymer Nanoparticles for NIR-IIa Fluorescence Imaging. *J Am Chem Soc* 2020;142(35):15146–15156. Available at: http://dx.doi.org/10.1021/jacs.0c07193